



## Microphysical properties and light absorption enhancement of refractory Black carbon aerosols in the central Arctic marine boundary layer: Role of warm airmass intrusions on mixing state

5 Babu Suja Arun<sup>1</sup>, Thomas Müller<sup>1</sup>, Mira L. Pöhlker<sup>1,2</sup>, Andreas Held<sup>3</sup>, Christopher Pöhlker<sup>4</sup>,  
Manuela van Pinxteren<sup>1</sup>, Yifan Yang<sup>1</sup>, Sabine Lüchtrath<sup>3</sup>, Andreas Walbröl<sup>5</sup>, Janna E.  
Rückert<sup>6</sup>, Philipp Oehlke<sup>1</sup>, Maik Merkel<sup>1</sup>, Birgit Wehner<sup>1</sup>

<sup>1</sup>Leibniz Institute for Tropospheric Research, 04318 Leipzig, Germany

<sup>2</sup>Leipzig Institute for Meteorology, University of Leipzig, Leipzig, Germany

<sup>3</sup>Environmental Chemistry and Air Research, Technische Universität Berlin, Berlin, Germany

10 <sup>4</sup>Max Plank institute for Chemistry, Mainz, Germany

<sup>5</sup>Institute for Geophysics and Meteorology, University of Cologne, Germany

<sup>6</sup>Institute of Environmental Physics, University of Bremen, Bremen, Germany

15 Correspondence to: Babu Suja Arun (arun.babu@tropos.de)

15

### Abstract:

Refractory black carbon (rBC) aerosol particles strongly influence Arctic atmospheric radiative transfer, making it essential to understand their microphysical properties and mixing state. However, in-situ investigations on microphysical properties and mixing state of rBC particles over the central Arctic marine boundary layer are 20 scarce. To address this gap, we carried out a comprehensive investigation of rBC particles in the central Arctic onboard the RV *Polarstern* during the ATWAICE cruise. Our results revealed pronounced spatial and temporal variability in microphysical properties rBC in the Arctic marine boundary layer, governed by transport pathways and removal mechanisms. Under pristine background conditions, rBC mass concentrations were at their lowest (median  $\sim 0.4\text{--}0.6 \text{ ng m}^{-3}$ ). Warm airmass intrusions into the Arctic atmosphere were found to bring polluted 25 anthropogenic aerosols into this pristine environment with an eightfold increase in rBC mass concentrations (median  $\sim 3.4 \text{ ng m}^{-3}$ ,  $\text{rBC}_{\text{max}} \sim 74 \text{ ng m}^{-3}$ ). A dominant influence of biomass-burning emissions from Eurasia during the warm airmass intrusion, which coincided with a shift toward larger rBC cores ( $\sim 264 \text{ nm}$ ) and moderate coating thickness. The light absorption enhancement of rBC remained low during warm-air-mass intrusions ( $\sim 1\text{--}1.2$ ) than under background conditions ( $\sim 1.1\text{--}1.6$ ), underscoring a strong dependence of rBC radiative effects in the central 30 Arctic on source regions and aging/processing during long-range transport. This study highlights the complexity of rBC aging and mixing state in the central Arctic, driven by variable source characteristics and summertime processing conditions and will help to increase the accuracy in representing rBC in climate models.



## 1. Introduction

35 The Arctic region is experiencing accelerated warming, a phenomenon known as Arctic Amplification. Over the past four decades, this has led to a nearly fourfold increase in surface air temperatures over the Arctic (Rantanen et al., 2022). Many climatic feedback mechanisms contribute to this process, involving interactions between the atmosphere, cryosphere, biosphere, and ocean. The key contributors to Arctic amplification include the decline in sea ice extent and thickness, changes in surface albedo, meridional atmospheric moisture transport, ocean heat

40 transport, and alterations in cloud characteristics (Woods and Caballero, 2016; Beer et al., 2020; Zhang et al., 2018; Thackeray and Hall, 2019; Wendisch et al., 2022). Although greenhouse gases are the primary driver of global warming, atmospheric aerosol particles significantly impact the Arctic climate by influencing the radiative balance through the scattering and absorption of solar radiation, cloud formation, and deposition processes (Haywood and Boucher, 2000; Schmale et al., 2021). The radiative impact of aerosols varies seasonally in the

45 Arctic, as cloud cover, surface reflectivity, and solar radiation fluctuate throughout the year (Quinn et al., 2008; Flanner, 2013). The Arctic aerosol life cycle is highly seasonal, primarily driven by long-range transport, atmospheric processing, and precipitation scavenging (Tunved et al., 2013). Elevated aerosol loadings were found during the Arctic haze period, when aerosol particles were primarily transported from industrialized regions of Eurasia and North America under stable atmospheric conditions (Stohl, 2006). During summer, Arctic aerosols

50 undergo extensive wet scavenging, while photochemical activity and biogenic emissions stimulate new particle formation (Engvall et al., 2008). Low-level clouds contribute to winter and early spring warming by trapping outgoing longwave radiation; whereas in summer, they exert a cooling effect by reflecting incoming solar energy (Zhao and Garrett, 2015). Light-absorbing aerosols can amplify these effects, raising atmospheric temperatures and potentially dissipating clouds (Sand et al., 2013).

55 One of the most significant climate-forcing aerosol components in the Arctic is black carbon (BC), which is produced by the incomplete combustion of fossil fuels and biomass (Bond et al., 2013). BC contributes to atmospheric warming mainly through three mechanisms: absorbing solar radiation (direct effect), altering cloud properties (indirect effect), and reducing snow and ice albedo when deposited on these highly reflective surfaces (albedo effect) (Flanner, 2013; Sand et al., 2013). Due to the limited number of local BC sources in the Arctic,

60 the majority of BC is transported from mid-latitude regions (Bozem et al., 2019; Croft et al., 2016; Gogoi et al., 2021; Pernov et al., 2022). BC transport into the Arctic lower troposphere is influenced by synoptic-scale circulation patterns and boundary-layer dynamics, with wet scavenging as the dominant removal mechanism (Garrett et al., 2011; Winiger et al., 2017).

65 The atmospheric lifetime, radiative impact, and cloud-interaction potential of BC aerosols are critically influenced by their microphysical properties, particularly size and mixing state (Ching et al., 2016; Asmi et al., 2025). Freshly emitted BC is typically hydrophobic and externally mixed. In contrast, during atmospheric transport, it undergoes aging via condensation and coagulation, acquiring coatings of organic and inorganic species that enhance its hygroscopicity and cloud condensation nuclei activity (Nenes et al., 2002; Motos et al., 2019a). This transformation not only alters the light absorption efficiency of BC but also modulates its susceptibility to wet

70 scavenging processes, especially nucleation scavenging within clouds (Matsui, 2016; Motos et al., 2019b). BC aging timescales are governed by atmospheric oxidant levels and precursor vapours, both of which vary seasonally



and regionally (Fierce et al., 2015). In the Arctic summer, despite higher photochemical activity, enhanced low-level cloudiness and fog formation may accelerate wet removal of aged BC, allowing relatively fresh or partially aged particles to dominate. Yet, the extent and rate at which BC becomes internally mixed in the Arctic marine boundary layer remain poorly understood. Understanding these microphysical transformations is essential to reduce uncertainties in Arctic BC radiative forcing, especially as climate models often simplify or misrepresent BC aging and removal processes (Ching et al., 2018).

Recent assessments have highlighted substantial uncertainties in Arctic BC emissions, primarily due to the underrepresentation of key sources such as gas flaring, waste burning, and mobile combustion in emission inventories (Schmale et al., 2018). For example, flaring emissions from northern Russia may contribute up to 66% of Arctic BC; however, isotope analyses suggest that this estimate may be too high due to errors in emission factors and spatial distribution (Winiger et al., 2017). Emission inventories vary by up to a factor of three (AMAP, 2015; Schmale et al., 2018), further compounding modelling uncertainties. In addition to emission uncertainties, the transformation of BC through atmospheric aging remains poorly constrained in Arctic conditions. This is particularly relevant in the Arctic MBL, where low temperatures and limited precursor gas concentrations slow BC aging (Fierce et al., 2016), and where summer fog and low-level cloudiness can enhance wet scavenging. Consequently, understanding how BC evolves microphysically, especially how it becomes internally mixed and activates as cloud condensation nuclei, remains a major knowledge gap. These microphysical changes critically influence the radiative efficiency of BC, its atmospheric lifetime, and its eventual deposition.

Despite advances in understanding Arctic aerosols, significant uncertainties remain in understanding BC aerosols and their climatic impacts, particularly regarding their interactions with clouds, transport pathways, and deposition processes, due to limited knowledge of the microphysical properties of BC. There exist long-term ground-based BC measurements from a network of Arctic observatories (e.g., Zeppelin, Ny-Ålesund, Pallas, Barrow, Alert, Tiksi, etc.) (Sharma et al., 2006; Eleftheriadis et al., 2009; Schmeisser et al. 2018; Gogoi et al. 2021), and in recent years numerous aerosol observations have also been made over the Arctic using ground-based stations, aircraft campaigns and shipborne platforms (Raatikainen et al., 2015; Schulz et al., 2019; Park et al., 2020; Jurányi et al., 2022, 2023; Zanatta et al. 2023; Heutte et al., 2023; Zieger et al. 2023). However, even now, the detailed understanding of the microphysical properties of refractory BC (rBC) particles remains scarce, especially in the central Arctic marine boundary layer (MBL). With this in mind, we have conducted the aerosol observations onboard RV *Polarstern* (PS131) in the central Arctic during summer 2022 to understand the microphysical properties and mixing state of rBC particles in the central Arctic MBL. This study investigates the size distribution, mixing state, and light-absorption enhancement, as well as the sources of rBC in the central Arctic MBL, with a particular focus on the role of warm air mass intrusions in modulating the microphysical properties of rBC.

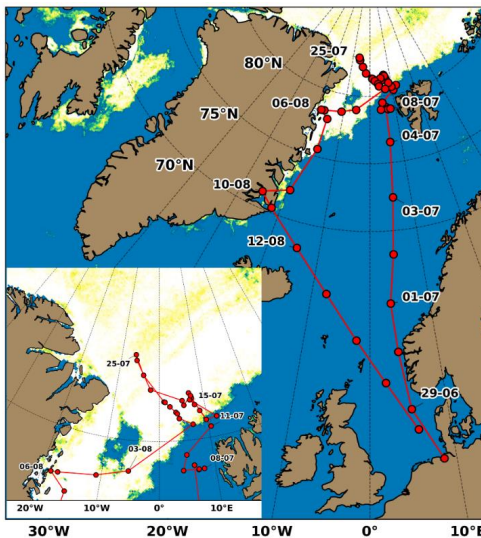
## **2. Experimental details**

### **105 2.1 Study region and general meteorological conditions**

Ambient atmospheric aerosol measurements were conducted over the Arctic Ocean aboard the icebreaker RV *Polarstern* (PS131), operated by Alfred Wegener Institute, Germany. The expedition PS131 named ATlantic WAtter pathways to the ICE in the Nansen basin and Fram Strait (ATWAICE) to the central Arctic, was carried



out during the summer period (28<sup>th</sup> June to 17<sup>th</sup> August, 2022), during which aerosol measurements were  
110 conducted from 29<sup>th</sup> June to 12<sup>th</sup> August. The ship track during the campaign is shown in Figure 1. The cruise  
covered the Arctic Ocean (including both the North Sea and the Greenland Sea) and the remote north-western  
Greenland Sea. *Polarstern* crossed the Arctic Circle during the night of 2<sup>nd</sup> July and proceeded towards the eastern  
Fram Strait, where it navigated between 5<sup>th</sup> and 10<sup>th</sup> July through the warm, saline waters of the west Spitsbergen  
current. By 11<sup>th</sup> July, *Polarstern* reached the continental slope north of Svalbard, continuing northwest into denser  
115 ice on 12<sup>th</sup> July. On 22<sup>nd</sup> July, *Polarstern* travelled northwest to the Gakkel ridge, reaching the expedition's  
northernmost point on 25<sup>th</sup> July. The southward transit towards the Fram Strait began on 2<sup>nd</sup> August. By 8<sup>th</sup> August,  
*Polarstern* arrived at Scoresby Sund, Greenland. More details about ATWAICE cruise and research area are  
provided in Kanzow et al. (2023).



120 **Figure 1:** Ship track of RV *Polarstern* during the ATWAICE cruise from 28 June to 17 August 2022. The red line indicates the cruise trajectory, with red circle symbols marking the ship's position at local noon each day. The inset shows a zoomed-in view of the northernmost cruise tracks.

Figure S1 illustrates the temporal evolution of meteorological parameters measured aboard RV *Polarstern* during the expedition. Wind speeds generally ranged between 4 and 14 m s<sup>-1</sup> during the observation period, with several  
125 transient peaks exceeding 12 m s<sup>-1</sup>, notably around 7<sup>th</sup> to 9<sup>th</sup> July, 16<sup>th</sup> to 18<sup>th</sup> July, and 6<sup>th</sup> to 8<sup>th</sup> August. At the beginning of the cruise, while the ship was in the sub-Arctic latitudes and the Norwegian Sea, air temperatures were relatively high (~10 °C to 18 °C), accompanied by moderate relative humidity (RH) values (~60-80%). As the vessel advanced northward into the marginal ice zone and eventually the central Arctic, a marked and sustained drop in temperature occurred beginning around 3<sup>rd</sup> to 5<sup>th</sup> July, stabilizing around or below 2-5 °C throughout much  
130 of mid-to-late July. During this same period, RH increased significantly, frequently exceeding 90%, indicating a colder, more saturated boundary layer consistent with ice-covered or near-ice environments. A notably colder and humid period is observed from approximately 23<sup>rd</sup> to 30<sup>th</sup> July, coinciding with the ship's passage through densely packed sea ice. Mid July (around 15<sup>th</sup> to 20<sup>th</sup> July) shows an interesting deviation from the preceding trend, marked by temperature increase (up to ~8 °C) and more variable RH, associated with a warm air mass intrusion over the



135 marginal ice zone. Toward the end of the cruise in early August, another warming phase is noted, particularly from 30<sup>th</sup> July to 3<sup>rd</sup> August, when the ship transitioned from ice-covered regions to open-ocean conditions. More details regarding the ATWAICE cruise are available elsewhere (Kanzow et al., 2023).

## 2.2 Measurements of aerosol particles

140 The measurements of aerosol particles were made from the specifically configured aerosol measurement container on the 'Peildeck' of the ship, with the instruments sampling the air from a common aerosol inlet. Nafion membrane aerosol driers were installed in the sampling lines to remove excess moisture, limiting the sampling relative humidity to < 40%. Measurements of rBC particles were performed using a Single Particle Soot Photometer (SP2, Model: SP2-D; Droplet Measurement Technologies, USA), which operates at 0.12 L min<sup>-1</sup>. SP2 utilizes the laser-induced incandescence technique to measure rBC properties using an Nd:YAG laser at 1064 nm (Schwarz et al., 145 2008). The amplitude of the incandescence signal from SP2 is proportional to the rBC mass present in BC-containing particles.

150 The leading-edge-only (LEO) fitting technique is commonly employed to reconstruct the scattering signal from SP2 (Gao et al., 2007; Liu et al., 2014) to understand the mixing state of rBC. The reconstructed signal is compared with Mie model values to derive the size of coated BC particles. In this approach, the particle is assumed to exhibit a concentric core-shell morphology, represented as a sphere with the core having a refractive index of 2.26 - 1.26i and the coating set at 1.5 + 0i (Moteki et al., 2010). The BC core diameter (D<sub>c</sub>) is estimated based on an assumed atmospheric BC density of 1.8 g cm<sup>-3</sup> (Moteki and Kondo, 2010), while the amplitude of the scattering signal provides information about the scattering cross section of the particles, which is used to derive the optical sizing of the particles. Prior to measurements, the SP2 was calibrated using Aquadag® black carbon standards, with a 155 correction factor of 0.75 applied to account for differences from ambient BC (Baumgardner et al., 2012; Laborde et al., 2012; Yang et al., 2025). The coating thickness of BC-containing particles is inferred by comparing the optical diameter (D<sub>p</sub>) and the D<sub>c</sub>.

The absolute coating thickness (CT) is estimated as,

$$CT = (D_p - D_c)/2$$

160 The mass median diameter (MMD) is determined by fitting BC core size distributions to a monomodal log-normal distribution function (Liu et al., 2019).

To understand the size-resolved coating thickness of rBC particles during the study period, the rBC particles were classified into an i x j grid with i bins for rBC core diameter and j bins for coating thickness. The total volume of rBC containing particles at each grid point is estimated as (Yang et al. 2025),

$$165 \quad Volume_{grid(i,j)} = \frac{\pi}{6} D_{p(i,j)}^3 N_{i,j} = \frac{\pi}{6} (D_{c,i} + 2 \times CT_j)^3 N_{i,j}$$

where D<sub>p</sub> represents the diameter of the rBC containing particle and N indicates the total number of rBC particles. More detailed information regarding SP2, data interpretation procedures, uncertainties, and caveats is available elsewhere (Liu et al., 2014; Moteki and Kondo 2010; Yang et al., 2025).



170 To quantify the impacts of rBC particles in the Arctic, we calculated the absorption enhancement factor ( $E_{abs}$ ) and mass absorption cross-section (MAC) of rBC particles using Mie theory, constrained by in situ single-particle measurements obtained with SP2 (Yang, 2024). The individual coating thickness was derived assuming a concentric core-shell geometry. To estimate absorption properties, we assumed that each rBC particle can be modelled as a homogeneous spherical core with a concentric, non-absorbing coating (e.g., sulfate or organics). The complex refractive index for the rBC core was set to  $1.95 + 0.96i$ , consistent with literature values for soot, 175 while the coating refractive index was taken as  $1.53 + 0i$  (Moteki et al., 2023; Schnaiter et al., 2005; Zhang et al., 2018). We used a Mie scattering code based on the core-shell solution of Bohren and Huffman (1998) to compute the absorption cross-section of each size bin, both for coated ( $C_{abs,coated}$ ) and bare ( $C_{abs,bare}$ ) rBC particles.

The absorption enhancement factor was then calculated as:

$$E_{abs} = \frac{C_{abs,coated}}{C_{abs,core}}$$

180 This reflects the increase in light absorption caused by the lensing effect of the non-absorbing coating.

In parallel, the mass absorption cross-section (MAC) was derived using,

$$MAC = \frac{C_{abs}}{M_{rBC}},$$

185 where  $M_{rBC}$  is the mass of the rBC core in each size bin. The MAC values were computed for both bare and coated particles, providing insight into how mixing modifies the specific absorption capacity of rBC under different atmospheric conditions. This enabled direct comparison across regimes with differing aerosol source histories, atmospheric aging states, and mixing conditions.

190 The measurements of equivalent black carbon (eBC) were performed using a multi-angle absorption photometer (MAAP), which measures transmitted and backscattered light from a particle-loaded filter (Petzold and Schönlinner, 2004). Although the MAAP directly measures the absorption coefficient, the results were converted to eBC mass concentration using a predefined mass absorption cross section. In general, eBC measurements were reported at a wavelength of 637 nm, following the recommendations of Müller et al. (2011). A correction factor of 1.05 was applied to account for systematic biases in the retrieval of eBC concentrations. Measurements of light-scattering coefficients were performed using an integrated Nephelometer (Aurora Ecotech 4000). More details regarding this instrument are available elsewhere (Müller et al., 2011).

195 In addition, aerosol particle sampling was conducted using a high-volume digital aerosol sampler mounted on the rooftop of the aerosol measurement container. After sampling, the samples were stored in aluminium boxes at -20 °C and transported to TROPOS, Leipzig, for further chemical analysis. To account for potential contamination during handling and transport, field blanks were prepared by loading the sampler at the sampling site without drawing air through the system. Measurements of organic carbon and elemental carbon were made using a Sunset 200 OC-EC analyser following the EUSAAR II TOT protocol (Birch and Cary, 1996). The concentrations of selected inorganic species were determined in filtered aqueous extracts (0.45 µm syringe filters, 50% of the filter extracted in 2 mL ultrapure water) using ion chromatography (ICS3000, Dionex, Sunnyvale, CA, USA), following the



methodology described by Müller et al. (2010). Regular instrument calibration and quality control procedures were implemented to ensure the accuracy and reliability of the analytical measurements.

205 Ship plumes were occasionally detected during the campaign. To ensure that aerosol measurements were not influenced by emissions from the ship's exhaust, the sampling inlet was installed ahead of the ship's engines. Despite this strategic placement, some data points were still affected by ship emissions and had to be filtered out before further analysis to obtain a dataset representing background aerosol concentrations. The following conditions led to data exclusion: Data points were removed when the relative wind direction ranged between 110°  
210 and 260°, as this wind pattern could carry exhaust emissions toward the sampling inlet. Measurements taken at wind speeds below 2  $\text{ms}^{-1}$  were discarded since weak winds can cause local turbulence, increasing the risk of exhaust contamination. Sharp increases or abrupt fluctuations in total particle number concentration were considered indicative of contamination and were therefore excluded. Any extreme spikes in the incandescence signal from SP2 were removed, as they were likely linked to ship exhaust plumes. For offline aerosol sampling,  
215 an automated pollution-avoidance system was used. This system, which continuously monitored relative wind direction, was integrated with the digital sampler to automatically halt the sampling pumps when airflow originated from the sector associated with ship exhaust contamination.

### 2.3 Thermodynamic measurements of the atmosphere

220 A Humidity and Temperature PROfiler (HATPRO) microwave radiometer (Rose et al., 2005) was deployed on the Peildeck, adjacent to the aerosol measurement container during the cruise. This instrument continuously measures atmospheric radiances emitted by water vapor, oxygen, and liquid cloud droplets, utilizing seven frequencies between 22 and 31 GHz along a water vapor absorption line and seven additional channels between 51 and 58 GHz within the oxygen absorption complex. With a high temporal resolution of approximately 1 s, HATPRO provides near-continuous monitoring of key atmospheric variables. The primary observational mode  
225 involved zenith-pointing measurements, enabling the retrieval of vertically integrated water vapor (IWV), liquid water path (LWP), and vertical profiles of temperature and absolute humidity following established methodologies (e.g., Walbröl et al., 2022). In a shorter observational mode for 15 consecutive minutes each hour, the instrument was observing the surface, and no measurements of the atmosphere were recorded. Additionally, boundary layer scanning at multiple elevation angles was conducted to enhance temperature profiling within the lower  
230 troposphere.

## 3. Results and discussion

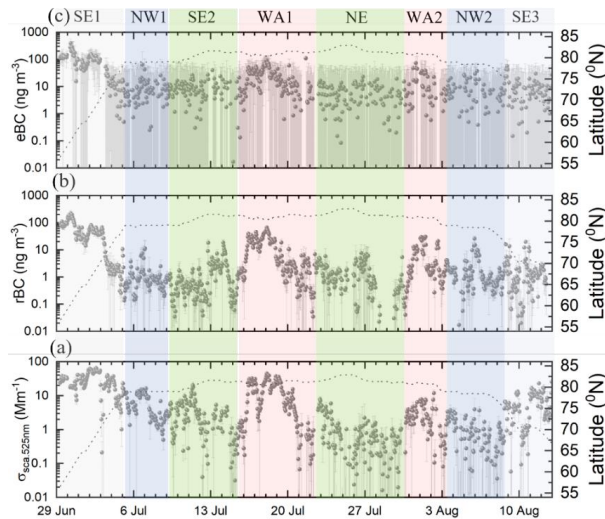
### 3.1 Latitudinal variability and source signatures of aerosol particles

235 Figure 2 provides an overview of the temporal and spatial variability of equivalent BC (eBC), refractory BC (rBC), and aerosol light-scattering coefficients at 525 nm ( $\sigma_{\text{sca}}$ ) observed along the latitudinal transect of the cruise track. Hourly  $\sigma_{\text{sca}}$  varies over a wide range (between 0.1  $\text{Mm}^{-1}$  and 66  $\text{Mm}^{-1}$ ) with ~90% of  $\sigma_{\text{sca}} < 25 \text{ Mm}^{-1}$ . The higher values of  $\sigma_{\text{sca}}$  during the beginning of the campaign is mainly associated with the proximity to the anthropogenic sources from the European continent. The  $\sigma_{\text{sca}}$  was generally low (<10  $\text{Mm}^{-1}$ ) in the high Arctic and increasing during transit toward lower latitudes, particularly south of 70°N. Episodic increases observed in  $\sigma_{\text{sca}}$



240 were potentially associated with long-range transported aerosols, biomass burning plumes or local sources such  
as sea spray aerosol emissions or marine biogenic emissions. As the *Polarstern* traversed northward,  $\sigma_{\text{sca}}$  values  
steadily declined and remained below  $5 \text{ Mm}^{-1}$  across large parts of the central Arctic region, which is consistent  
with the typically low aerosol loading in this region during summer (Schmeisser et al., 2018; Pandolfi et al. 2018;  
Gogoi et al., 2021). Several earlier studies reported the large spread of light scattering coefficient during the  
Arctic summer period associated with the sea spray aerosols, biogenic emissions, as well as the anthropogenic  
influx from Europe (Quinn et al., 2002; Tomasi et al., 2007; Schmeisser et al., 2018; Schmale et al., 2022).

245



250

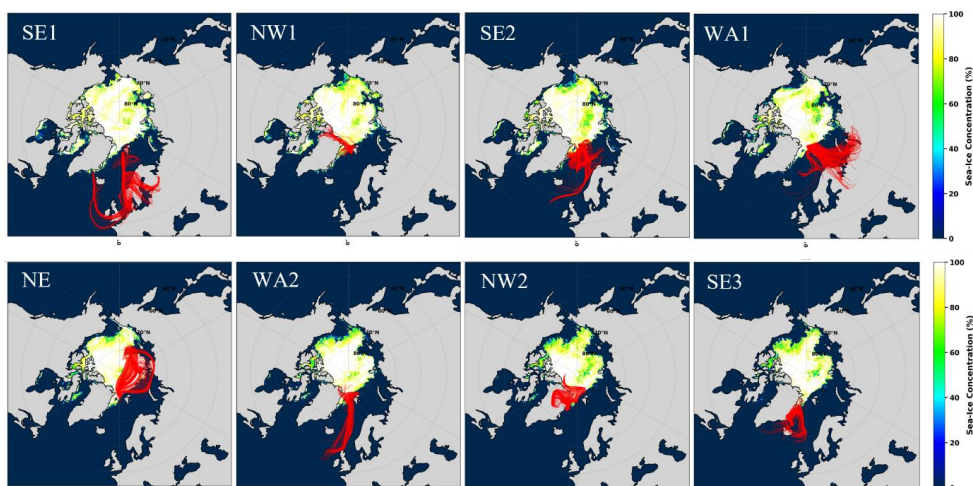
**Figure 2:** (a) Light scattering coefficient of aerosols measured at wavelength 525 nm, (b) Refractory black carbon  
mass concentration measured using SP2, (c) Equivalent Black carbon mass concentration measured using MAAP.  
Each subplot is accompanied by a dotted line indicating the corresponding latitude (right y-axis). The vertical  
grey lines indicate the respective standard deviation for each parameter.

255

eBC and the mass concentration of rBC ( $M_{\text{rBC}}$ ) also showed significant temporal variability, particularly during  
the beginning of the cruise (29<sup>th</sup> June to 3<sup>rd</sup> July), when the ship was positioned at comparatively lower latitudes.  
During this period, eBC frequently exceeded  $100 \text{ ng m}^{-3}$  and even reached  $399 \text{ ng m}^{-3}$ , indicating the influence of  
the proximity to the European continental/ship emission sources. Northward of  $70^{\circ}\text{N}$ , starting in early July, eBC  
concentrations declined markedly, with 95% of the values remaining below  $40 \text{ ng m}^{-3}$  for the rest of the cruise.  
This northward decline underscores the relatively clean and isolated nature of the high Arctic atmosphere in  
summer. The temporal trend of rBC follows that of eBC, with elevated concentrations observed in the sub-Arctic  
and much lower values in the central Arctic. During the central Arctic transect (approximately 10<sup>th</sup> to 27<sup>th</sup> July),  
both eBC and rBC mass concentrations remained consistently low, indicative of background conditions over sea  
ice and the open ocean. The measured mass concentrations range aligns well with previously reported values from  
various Arctic field campaigns (Taketani et al., 2016; Schulz et al., 2019). Nonetheless, episodes of enhanced  $\sigma_{\text{sca}}$ ,  
eBC, and rBC were observed from 15<sup>th</sup> to 22<sup>nd</sup> July and 30<sup>th</sup> July to 3<sup>rd</sup> August, suggesting the transient influence  
of warm airmass intrusions favourable for enhanced aerosol loadings. This will be discussed in detail in section

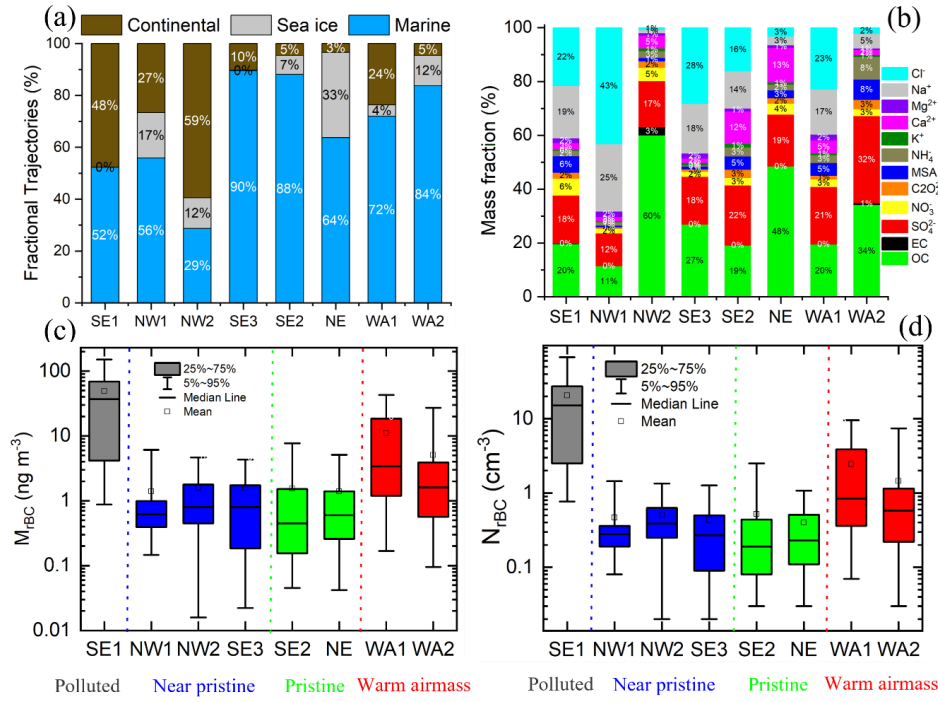


3.2. The observed differences in magnitude and variability of  $M_{rBC}$  and eBC, likely reflecting both instrumental  
265 differences and variability in aerosol composition (Backman et al 2017; Asmi et al. 2021, 2025). Further, we  
observed that elemental carbon (EC) concentrations derived from aerosol filter samples were mostly below the  
detection limit of the OC-EC analyzer throughout the cruise (Figure S2). This highlights the limitations of filter-  
based techniques in capturing low EC loadings, which are typical of the clean Arctic environment. However,  
270 single-particle measurements with the SP2 provide highly sensitive, real-time rBC that is more reliable under such  
conditions. To better explain the properties of BC, we will focus on rBC in the remaining discussions.



275 **Figure 3:** Backward airmass trajectories arriving at the ship position during the campaign segregated into different continuous airmass regimes (SE1- South easterly 1, NW1- North westerly 1, SE2- South easterly 2, WA1- Warm airmass intrusion 1, NE- North easterly, WA2- Warm airmass intrusion 2, NW2- North westerly 2, SE3- South easterly 3) during the study period.

In order to understand the spatio-temporal variabilities in rBC and its sources, airmass trajectory analysis were carried out. Figure 3 shows five days backward airmass trajectories arriving at the ship's position (~100 m a.s.l) estimated using NOAA Hybrid Single-Particle Lagrangian Integrated Trajectory model (HYSPLIT) (Stein et al., 2015) overlaid on the Arctic Sea ice concentration data from MODIS-AMSR2 (Spreen et al., 2008; Ludwig et al., 280 2020) during the cruise period. These trajectories are grouped into eight consecutive regimes (SE1- South easterly 1, NW1- North westerly 1, SE2- South easterly 2, WA1- Warm airmass intrusion 1, NE- North easterly, WA2- Warm airmass intrusion 2, NW2- North westerly 2, SE3- South easterly 3) based on the dominant directions of airmasses arriving at the ship's position. This allows us to identify key transport pathways and surface-type interactions (open ocean, sea ice, continental) relevant to the observed variability in rBC properties during the cruise. Further, we have analysed the residence time of each airmass under distinct surface types, such as continental (indicating airmass transport through continental landmasses), marine (indicating airmass transport through open ocean waters), and sea ice (representing airmass transport over sea ice). Figure 4(a) shows the percentage contribution of each of these surface type contributions for the airmasses under consideration in this study.



290

**Figure 4:** (a) Stacked bar plots representing the fractional contributions of three different surface types traversed by air masses before arriving at each of the eight designated airmass sectors: SE1, NW1, NW2, SE3, SE2, NE, WA1 and WA2. The three categories are: Marine (Blue): Air masses that predominantly travelled over oceanic regions. Sea Ice (Gray): Air masses that passed over areas covered by sea ice. Continental (Brown): Air masses influenced by land surfaces. Each bar is segmented and annotated with percentage values indicating the proportion of time the air masses spent over each surface type before reaching the measurement location, (b) mass fraction of chemical species estimated from offline aerosol measurements, (c) Box and whisker diagram showing the variabilities in mass concentration of refractory BC, (d) number concentration of rBC particles in each study regimes.

300 The analysis revealed distinct spatial heterogeneity in aerosol properties, particularly rBC, linked to distinct airmass origins. The SE1 regime originated mainly over continental Europe, traversing predominantly marine pathways, including the North Atlantic Ocean and the North Sea, with significant anthropogenic influence (Figure 4a). These trajectories passed through industrialized regions and major shipping corridors before entering the Arctic. Correspondingly, SE1 exhibited the highest rBC mass concentrations observed during the campaign 295 (median  $\sim 37$  ng m<sup>-3</sup>) (Figure 4c). This points to efficient long-range transport of combustion-derived aerosols and their sustained presence in marine-urban mixed air masses, in addition to direct exposure to aerosol loading. The SE1 regime allows us to compare pristine central Arctic conditions with polluted oceanic conditions. Further, we have noted an enhanced contribution of sea-salt aerosols during this period, as indicated by the dominant contribution of Na<sup>+</sup> and Cl<sup>-</sup> ( $\sim 41\%$ ) to the chemical composition (Figure 4b). This could further contribute to the 305 enhanced light scattering coefficient ( $\sim 36$  Mm<sup>-1</sup>) observed during this period. In contrast, the SE2 and SE3 regimes 310



reflect a more remote marine influence (SE2 ~88%, SE3 ~90%). SE2 air parcels mostly traversed through the Barents Sea and the adjacent Arctic Ocean, traveling over open water and marginal ice with minimal continental contact. The rBC concentrations during this regime were among the lowest (~0.45 ng m<sup>-3</sup>), reflecting limited contributions of anthropogenic sources. SE3 trajectories, although marine-dominated, originated from the  
315 northern Atlantic sector, including the Barents and Norwegian Seas. Even though these air masses did not have much contact with continental landmasses, they likely encountered oceanic regions affected by background European outflow or by shipping emissions. As such, rBC levels in SE3 were modest (mean ~0.8 ng m<sup>-3</sup>), slightly higher than SE2 but well below SE1, and could represent moderately aged marine aerosols.

The NE regime, encountered at the northernmost latitudes of the cruise, is significantly influenced by air parcels  
320 transported from the central Arctic Ocean over consolidated sea ice conditions (>30% concentration). These air masses were effectively isolated from both continental and lower-latitude marine regions, exhibiting the lowest aerosol concentrations. The rBC levels were consistently minimal (<0.6 ng m<sup>-3</sup>), and the light scattering coefficients were similarly lower ( $\sigma_{sca}$  ~1 Mm<sup>-1</sup>). The lower scattering coefficients could also be influenced by the  
325 minimal contribution of marine emissions to light scattering, since sea spray emissions are lower than in open ocean waters. These observations reflect the near-pristine Arctic background state, shaped by slow-moving air masses under cold, stable boundary layer conditions with minimal vertical or horizontal mixing.

NW1 and NW2 showed mixed marine-continental influences. NW1 trajectories originated over northern Greenland, moving over both land and the Greenland Sea before reaching the ship position near the MIZ. The combined land and ocean exposure during this period suggests moderate loadings of aerosol particles from natural  
330 sources (e.g., glacial dust, re-suspended particles) and possibly aged Arctic background conditions. The rBC concentrations were similar to the concentrations in the NE regime (median ~0.8 ng m<sup>-3</sup>). However, NW2 showed an unexpectedly high proportion of continental influence (~59%) based on trajectory surface-type classification, despite having lower rBC concentrations (~0.8 ng m<sup>-3</sup>). The source region is mostly sea-ice-covered areas north of Greenland and the Fram Strait, suggesting that continental influence here likely came from earlier stages of  
335 transport or from the entrainment of aged aerosol layers that had already been scavenged en route. Schmale et al., (2018) noted that interactions among marine, ice-covered, and continental surfaces critically influence aerosol composition and aging in the central Arctic region. Air masses traveling over industrialized zones or biomass-burning regions tend to carry elevated BC and associated pollutants, while those traversing the open ocean or consolidated ice generally yield background or near-pristine conditions. The aging timescale of BC particles is  
340 longer in the Arctic due to sparse precursors and limited secondary processing, making the central Arctic MBL particularly susceptible to prolonged periods of low aerosol concentrations, especially in the absence of active transport (Schmale et al., 2018). In addition, the lowest rBC concentrations in the central Arctic during the summer period are influenced by efficient scavenging processes due to the thick layers of fog observed during the summer Arctic period.

345 Earlier, Taketani et al. (2016) reported pronounced spatial variability in rBC between the North Pacific and Arctic oceans in September, with mass concentrations ranging from 0 to 60 ng m<sup>-3</sup> and an average of about 1 ng m<sup>-3</sup>. Schulz et al. (2019) measured rBC in the Canadian Arctic during summer and showed that combustion-derived particles constituted only a minor fraction of the aerosol population. They noted that near-surface rBC



concentrations were typically less than  $2 \text{ ng m}^{-3}$  and that the summer polar dome had little exchange with mid-latitude air masses. Our observed rBC concentrations are lower than those reported by Liu et al. (2015) in the European Arctic during spring, where rBC mass concentrations ranged from 20 to  $100 \text{ ng m}^{-3}$ , as expected given the general shift toward lower rBC levels from spring to summer. Based on the airmasses histories and the rBC concentrations, we have segregated the distinct regimes as, polluted (SE1), near-pristine (NW1, NW2 and SE3), pristine (SE2 and NE) and warm airmass intrusions (WA1 and WA2).

355 **3.2 Warm airmass intrusions and refractory BC**

We observed noticeable warm air-mass intrusions into the central Arctic Ocean during the study period, which disrupted the aerosol budget during the expedition. The events caused significant changes in the aerosol properties within a few days, transforming the Arctic from a remote, low-particle environment to conditions more similar to a continental setting in Europe. Recent years have seen an increase in the frequency and duration of these synoptic-scale intrusions, which are brief but intense episodes linked to large-scale blocking (Graham et al., 2017, Mortin et al., 2016; Henderson et al., 2021; Dekoutsidis et al., 2024).

The temperature and absolute humidity profiles retrieved from HATPRO are shown in Figure 5. Between 13<sup>th</sup> and 14<sup>th</sup> July, an occluded warm front associated with a low-pressure system over the North Atlantic transported warm and moist air. Temperatures reached up to  $7^\circ \text{C}$  (at approximately 600 m altitude) during this phase. Subsequently, 365 with the start of regime WA1, two pronounced intrusions of warm and humid air were observed from 15<sup>th</sup> to 17<sup>th</sup> July and 17<sup>th</sup> to 19<sup>th</sup> July, caused by two consecutive low-pressure systems approaching south of Svalbard. Strong south easterly winds carried significant moisture toward Svalbard and adjacent areas (Kanzow et al., 2023). The second low was especially powerful, with temperatures peaking at  $18^\circ \text{C}$  (at 650 m altitude) on 18 July and a maximum recorded integrated water vapor of  $35 \text{ kg m}^{-2}$  which is untypically high for polar regions. During these 370 events, *Polarstern* was mostly in open water on the lee side of Svalbard. On 19<sup>th</sup> July 2022, a third warm air advection event occurred; however, it was weaker than the previous two events and was not accompanied by a significant increase in humidity. A weak high-pressure system led to persistently foggy and cloudy conditions, with some warm air inflow in the two consecutive days. During regime WA2 (30<sup>th</sup> July to 3<sup>rd</sup> August), as 375 *Polarstern* began its transit toward the east coast of Greenland into a warm front, warm air masses were observed, with temperatures reaching up to  $8^\circ \text{C}$  at 850 m altitude and integrated water vapor increasing from 14 to  $22 \text{ kg m}^{-2}$ . Near the surface, temperatures remained close to  $0^\circ \text{C}$ , accompanied by persistent fog. For further discussion 380 of aerosol properties, we considered the warm airmasses from 15<sup>th</sup> to 22<sup>nd</sup> July as WA1 and from 30<sup>th</sup> July to 03<sup>rd</sup> August as WA2.

The two regimes, WA1 and WA2, considered in this study represent warm air mass intrusions from the southeast, 385 with differing source characteristics. The elevated mass concentrations measured during warm air mass intrusions indicate a strong influence of mid-latitude pollution advected into the central Arctic Ocean. WA1 is marked by strong continental outflow from Eurasia with strong passage over the Barents Sea towards the central Arctic. This Barents-sector pathway is widely regarded as the most effective corridor for carrying pollutants from northern Eurasian source regions into the Arctic (Stohl et al., 2013). A smaller subset of air masses was also passing over the Norwegian Sea. The air masses associated with WA1 were observed to affect regions known to contribute



pollutants to the Arctic, particularly through gas flaring and metallurgical industrial sources (Stohl et al., 2013; Schulz et al., 2019; Dada et al., 2022). Further, we have noticed that the trajectories during WA1 passed directly over fire-dense regions, as confirmed by MODIS Visible Infrared Imaging Radiometer Suite (VIIRS) satellite data fire-pixel counts, as shown in Figure S3. In addition, during WA1, we observed a significant increase in  $K^+$ ,  
390 which supports the predominant role of biomass burning during this period over the central Arctic Ocean. Therefore, we suggest that during WA1, *Polarstern* was strongly impacted by a mix of biomass burning sources and gas-flare emissions. As a result, rBC mass concentrations reached as high as  $74 \text{ ng m}^{-3}$ , and the observed mass concentrations were nearly eightfold (median  $\sim 3.4 \text{ ng m}^{-3}$ , rBC number concentration  $\sim 0.84 \text{ cm}^{-3}$ , Figure 4c-d), higher than those observed in the preceding period of observations (SE2). This episode demonstrates the ability  
395 of warm intrusions to deliver biomass burning aerosols deep into the Arctic marine boundary layer. These observations were aligned with previous findings that underscore the efficiency of synoptic-scale transport in delivering anthropogenic and biomass-burning aerosols into the Arctic lower troposphere (Dada et al., 2022). The variability in rBC observed within WA1 points to the advection of various anthropogenic air masses and varying vertical mixing, which may be coupled with washout during long-range transport and/or secondary processing, as  
400 observed, similar to the overall aerosol properties observed during warm airmass intrusions by Dada et al. (2022).

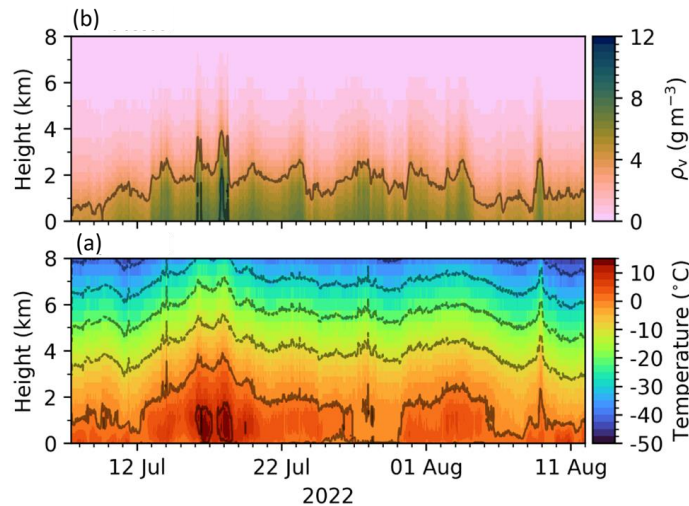


**Figure 5:** (a) HATPRO microwave radiometer retrieval of air temperature (K) vertical profiles, (b) absolute humidity from HATPRO.

The BC concentrations measured under near pristine and pristine conditions fall within the range typically reported for the Arctic summer (AMAP, 2015; Zanatta et al., 2023; Jurányi et al., 2023). In contrast, the markedly enhanced BC levels during WA1 (eBC as high as  $111 \text{ ng m}^{-3}$ , rBC as high as  $74 \text{ ng m}^{-3}$ ), while clearly elevated relative to background, remain lower than values observed during warm air-mass intrusions in spring (Dada et al., 2022), in subarctic environments, and in near-source high-Arctic sites (Popovicheva et al., 2017). It is also important to note that those studies quantified equivalent BC using an Aethalometer; differences in measurement  
405 technique may therefore influence comparisons of absolute BC magnitudes. In contrast, WA2 represents clean marine inflow from the North Atlantic or Norwegian and Greenland seas, moving north through the Fram  
410



Strait/western Barents MIZ, with minimal continental (land) influence before arriving at the position of the *Polarstern*. The rBC mass concentration reached as high as  $35 \text{ ng m}^{-3}$  during this period (median  $\sim 1.6 \text{ ng m}^{-3}$ , rBC number concentration  $\sim 0.58 \text{ cm}^{-3}$ ), which is comparatively lower than WA1, reflecting the influence from aged marine air enriched with enhanced sulfate and OC (Figure 4b).

### 415 3.3 Size distribution of refractory BC particles

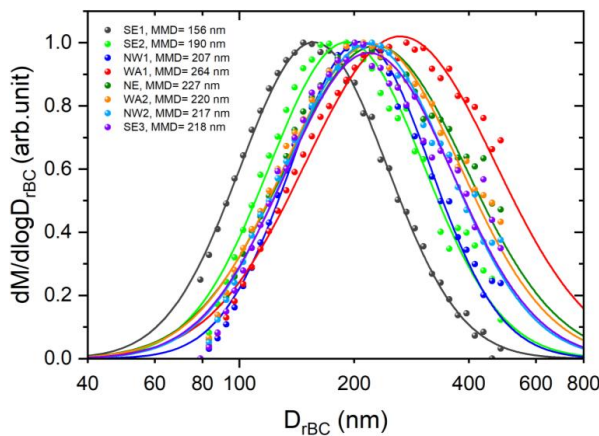


**Figure 6:** Mass size distribution of refractory black carbon particles estimated during the ATWAICE cruise during distinct airmass conditions.

420 The light-absorption properties of rBC aerosols are directly related to their size distribution, which is influenced by sources, sinks, and transformation processes during atmospheric long-range transport (Liu et al. 2019). Previous studies have demonstrated that rBC cores emitted from fossil fuel combustion sources typically exhibit smaller MMDs than those from biomass and biofuel burning (Shiraiwa et al., 2007; McMeeking et al., 2010; Liu et al., 2014; Taylor et al., 2014; Kompalli et al., 2020, 2021; Yang et al., 2025). Figure 6 shows the mass size distribution of rBC particles estimated for different airmass regimes during the study period.

425 During SE1, the estimated MMD is  $\sim 156 \text{ nm}$ , which resembles values typically observed in urban environments influenced by dominant fossil fuel emission sources (Laborde et al., 2013; Liu et al., 2019; Kompalli et al., 2020; Lim et al., 2023). As discussed before, this period was predominantly influenced by European continental outflow, a major source of fossil-fuel combustion emissions that generally produce smaller rBC cores. As the ship 430 transitioned to NW1, the MMD gradually increased to  $\sim 190 \text{ nm}$ , influenced by the changes in airmass characteristics. As the vessel continued towards SE2 in the MIZ, the MMD further increased to  $\sim 207 \text{ nm}$ , with air masses originating predominantly from the south-eastern oceanic sectors north of Europe. MMD increased further (MMD  $\sim 225 \text{ nm}$ ), as the ship advanced into the higher latitude packed ice conditions. This is associated with air masses predominantly from the northeast, traversing extensively over sea ice. Air masses originating from the 435 northwest (Greenland region) during NW2 resulted in an MMD of  $\sim 217 \text{ nm}$ . As the ship entered the Greenland zone, the MMD remained similar as NW2 ( $\sim 218 \text{ nm}$ ), despite a shift in airmass transport from south-easterly flow. The observed MMDs clearly show an increase in rBC cores across latitudes from Europe to the central Arctic.



This increase in MMD suggests a reduced influence from fossil fuel sources and a dominant role for biomass burning emissions in the central Arctic region via long-range atmospheric transport.

440 Interestingly, we noticed an enhancement in the MMD of rBC particles (~264 nm) during the warm airmass intrusion (WA1). This clearly indicates that biomass burning aerosol particles were transported to elevate the MMD of rBC during this period, as discussed before, with the enhanced rBC contribution heavily associated with intense biomass burning aerosols from Eurasia, in addition to gas flare emission sources. Further, during the warm airmass intrusion during WA2, the MMD of rBC remained ~220 nm, similar to typical central Arctic conditions,  
445 as discussed earlier. It should be noted that the airmass during WA1 contributed by landmass was ~23%, whereas during WA2 it was only ~6%, with little influence from biomass-burning source regions. This clear distinction in the MMD of rBC particles in the central Arctic indicates that the MMD of rBC particles is primarily dependent on the characteristics of the source region. Relative to background conditions, the intrusion exerted a strong influence on both the rBC mass loading and the microphysical properties of rBC aerosols in this remote Arctic  
450 Ocean. This in contradiction with previous studies, which reported that warm airmass intrusions do not affect the microphysical properties of aerosols in the central Arctic (Dada et al., 2022).

455 The MMD of rBC may change during long-distance transport as the particles undergo atmospheric processing. Larger BC cores are more effectively removed by wet scavenging, which can push the MMD toward smaller sizes because the air mass may encounter clouds and precipitation during transport (Moteki et al., 2012; Schulz et al.,  
460 2019). However, coagulation may occur as particles age, potentially shifting the distribution toward larger sizes (Tunved et al., 2013). This indicates that atmospheric processing during transport, in addition to the emission source, shapes the rBC mass-size distribution we observe (Schulz et al., 2019). This is particularly crucial in the Arctic because cloud-driven removal and BC transport into the area can happen simultaneously and support one another (Liu et al., 2011). Because of this, the size distribution of rBC alone hardly provides a fingerprint of the primary removal mechanism or the dominant source type. Our observed MMD values are higher than those reported for the high Canadian Arctic by Schulz et al. (2019), who found rBC MMDs in the range of 119-134 nm. In addition, our observed MMD values are higher than those observed in summertime measurements over the North Pacific Ocean, the Bering Sea, and the Arctic Ocean, where MMDs varied from 168 to 192 nm (Taketani et al., 2016). Earlier, Liu et al. (2015) reported an MMD of ~190 -210 nm during spring during the ACCACIA campaign. Zanatta et al (2018) reported rBC MMD of ~ 240 nm during spring in the Zeppelin observatory.  
465

### 3.4 Mixing state of refractory BC containing particles

470 Figure 7 shows the size resolved coating thickness of rBC particles estimated during the study period, along with the volume of rBC particles. The size resolved coating thickness (CT) of rBC particles, along with the number concentration of particles is given in the supplementary Figure S4. The size-resolved CT provides a more direct insight into the mixing state of rBC particles.

It is evident that, throughout the study period, two distinct regions consistently exhibited high volumes of coated rBC. However, higher volumes of coated rBC in the lower size range (<120 nm) are observed during SE1 and WA1. This shows the capability of warm airmass intrusions to bring higher abundances of coated rBC particles in smaller size ranges to the central Arctic, similar to regions highly influenced by continental anthropogenic



475 exposures. The bottom-left region with null values corresponds to smaller rBC particles that show neither positive nor negative coating thickness (CT), due to the detection limitations of the SP2 instrument, as reported in several studies (Ko et al., 2020; Yang et al., 2025). This detection limitation restricts the retrieval of coating information from scattered light for smaller rBC particles. As a result, the mixing state of a substantial portion of these small rBC particles remains unresolved. The average CT estimation may be skewed by the lack of CT details for smaller  
480 rBC particles. Only coated rBC particles with rather thick coatings are found for particles smaller than 150 nm, leading to an overestimation of the mean CT.

It is interesting to note a higher volume of rBC with core sizes >150 nm, except for SE2 and SE3. It is found that, although these two regions are influenced by southerly airmasses, they are mostly transported over open ocean regions, as evident from Figure 4(a). The lower contribution of continental airmasses (~5%) in comparison with  
485 relatively higher contribution of continental airmasses (~10%) could have contributed to relatively higher coated particles to SE3. Further, regions with higher volumes of rBC with core sizes >150 nm are prominent during NW1, NW2 and NE. The difference in the proportion of non-BC material among BC-containing particles of different core sizes can be defined as mixing-state heterogeneity, as previously reported in several studies (Zeng et al., 2024; Zhai et al., 2022). This heterogeneity is critical in understanding the absorption enhancement of coated  
490 rBC (Fierce et al., 2016; 2020; Zeng et al., 2024).

In order to provide a statistical insight into the mixing state information of rBC particles, the frequency distribution of CT estimated in the 180–300 nm is shown in Figure 8. The median CT for the near pristine, pristine and warm airmass conditions during the study varied from 14–18 nm, 9–20 nm and 12–15 nm. It is found that coating thickness was relatively higher in regions influenced mainly by northerly air mass advections (NE, NW1 and  
495 NW2, with  $CT_{median} \sim 20$  nm and  $CT_{median} \sim 18$  nm, and  $CT_{median} \sim 18$  nm respectively), while the lowest coating thickness is found during SE2 ( $CT_{median} \sim 9$  nm). The lower SE2 coating thickness compared to SE1, despite larger rBC cores, suggests less photochemically processed aerosols or lower availability of condensable materials in this relatively clean, higher-latitude region. Further, the lower coating thickness at SE2 could also be due to higher cloud scavenging during this period, as evidenced by denser fog layers associated with lower visibility (Kanzow  
500 et al. 2023) during SE2.

In northerly airmass regimes, these air masses likely experienced prolonged atmospheric residence times and active secondary aerosol condensation, leading to more internally mixed, coated rBC particles. Specifically for the northerly airmasses, we observed a higher fractional contribution to the total aerosol mass (Figure 4b) from sulfate ( $SO_4^{2-}$ , ~18%) and organics (OC, ~48%) especially during NE. The prolonged transport through marine  
505 and sea ice covered environments (Figure 4a) and the associated extended atmospheric aging of rBC particles during NE could have facilitated the condensation of secondary species onto rBC cores. However, for the NW2, particularly when the ship was located in the Greenland Sea, the contributions from  $SO_4^{2-}$  and OC were even higher. These increased fractions of organics and sulfate may have contributed significantly to the observed enhancement in the coating of rBC cores during this period. It is important to note that the NE regime was  
510 predominantly influenced by air masses traversing oceanic and sea-ice-covered regions, whereas the NW2 regime was more strongly affected by continental outflow from Greenland. However, because simultaneous real-time submicron aerosol chemical composition measurements are not available alongside rBC data, we cannot definitively attribute the enhanced coating to these chemical species. Furthermore, the fractional contributions



shown in Figure 4b are derived from daily  $PM_{10}$  filter samples, which may introduce biases while interpreting SP2  
515 derived coating thicknesses, as the SP2 specifically measures submicron aerosols.

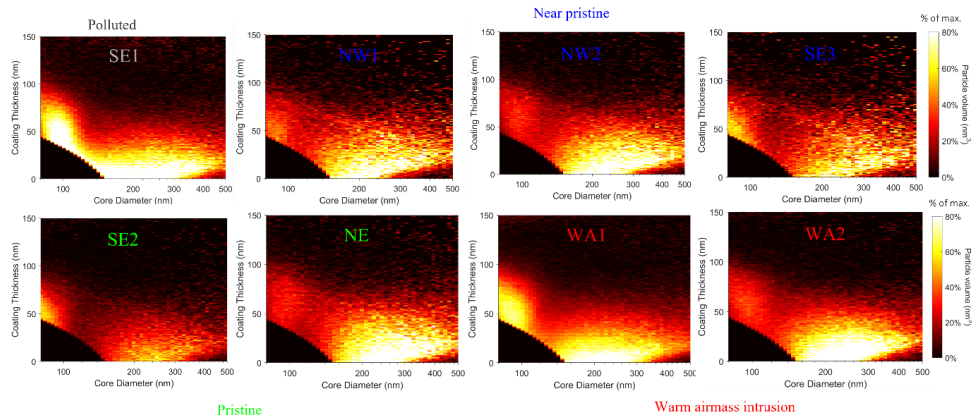


**Figure 7:** Size segregated coating thickness of rBC particles during the campaign. The colour bar indicates the particle volume (in percentage) in each size bin.

During the WA1, the median CT is  $\sim 12$  nm. This suggests that warm-air mass intrusions have a notable influence  
520 on the coating of rBC particles, as evidenced by the difference in CT between SE2 (prior to the warm-air mass intrusion) and WA1. This difference could be attributed to the presence of aged rBC particles transported into the central Arctic during these intrusions from biomass-burning sources, as discussed before. During WA2, as the ship re-entered the marginal ice zone, it was influenced by a short-lived warm airmass advection from the southeast, which primarily passed over oceanic regions. The estimated median CT during this period is  $\sim 15$  nm,  
525 which is relatively high compared to WA1. Interestingly, during the second warm airmass intrusion, the prevailing air masses shifted from north-easterly to south-easterly, which could have contributed to the observed changes in coating thickness. CT, along with a relatively higher contribution of airmasses traversing open oceanic regions, suggests relatively aged rBC particles during WA2. This could have significantly influenced the observed changes in CT between WA2 and WA1, where continental emissions and biomass-burning sources were more prominent.  
530 In addition, we noticed that the mass fractions of  $SO_4^{2-}$ ,  $NH_4^+$ , MSA, and  $C_2O_4^{2-}$  were higher during WA2 than during WA1. Further, we found significant correlations between  $NH_4^+$  and  $SO_4^{2-}$  ( $R^2=0.5$ ),  $SO_4^{2-}$  and MSA ( $R^2=0.4$ ),  $C_2O_4^{2-}$  and  $NO_3^-$  ( $R^2=0.6$ ), indicating significant SOA formation/photochemical aging of aerosols during this period. This further supports the aged nature of the aerosols, which are likely to have contributed to the relatively higher CT during WA2.  
535 Despite evidence of long-range transport, rBC particles exhibited thin to moderate coatings, unlike previous observations in background environments with thickly coated rBC particles (Motos et al., 2020; Yang et al., 2025). This infers lower precursor gas concentrations and limited condensation under summer Arctic conditions, where clean background air and reduced SOA formation can suppress coating even on aged rBC particles. Additionally, in-cloud and below-cloud scavenging, especially during the prevalent fog and low-level cloud conditions of Arctic  
540 summer, likely play a significant role in removing hydrophilic or heavily coated rBC particles. Although photochemical activity does occur in summer, the persistent presence of clouds and fog enhances wet scavenging, which disproportionately affects more processed aerosols. This effect is particularly evident in our observations



from warm air mass intrusions (WA1), which, despite being associated with biomass burning and continental sources, showed significantly larger rBC cores (MMD > 260 nm) but surprisingly thinner coatings than background air masses, such as those from the NE and NW sectors. These background regimes, dominated by air masses traversing marine or consolidated sea-ice regions, featured moderately large rBC cores (MMD ~220 nm) with moderate coatings, suggesting the combined influence of aerosol aging and active wet scavenging. The low coating thicknesses observed in the southeast sector (e.g., SE2), despite large MMDs, indicate that particle aging alone does not guarantee thicker coatings; rather, prevailing environmental conditions, such as low oxidant levels or cleaner marine airmasses, can suppress coating.

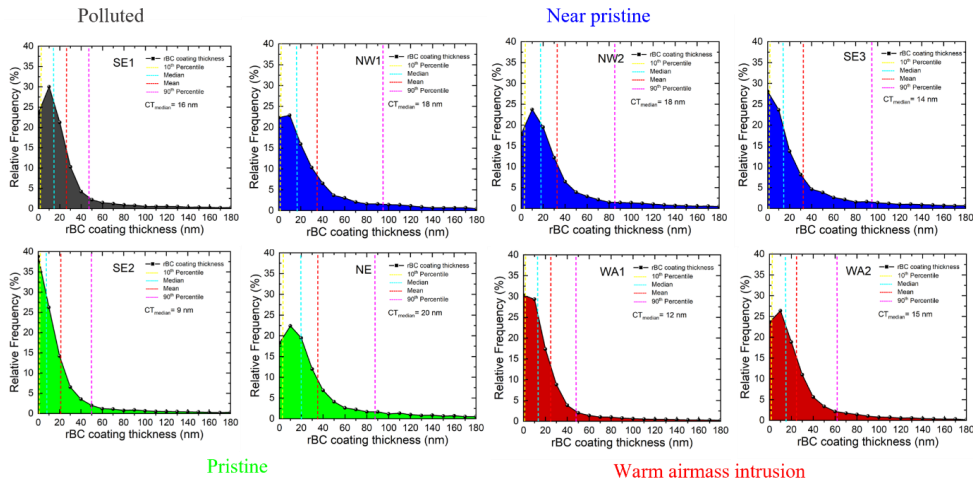


**Figure 8:** Frequency distribution of the coating thickness histograms during the study period for each airmass regimes for the rBC core size range of 180–300 nm.

### 3.5 Light absorption enhancement of rBC particles

To understand the role of microphysical properties and mixing state on light absorption enhancement, we have quantified the light absorption enhancement ( $E_{abs}$ ) and mass absorption cross-section (MAC) of rBC particles using Mie theory, constrained by in-situ single-particle observations obtained using SP2 as discussed in section 2.2.  $E_{abs}$  quantifies the increase in light absorption due to the presence of non-absorbing coatings on BC particles, relative to uncoated (bare) BC. For smaller core sizes, even modest coatings can result in substantial enhancement due to the strong lensing effect. However, as the core size increases, the relative impact of coatings on absorption enhancement diminishes. Figure 9 presents the size-resolved  $E_{abs}$  and MAC of rBC particles during the study period.

Across all air mass regimes, the size segregated  $E_{abs}$  values range from ~1 to 2.8 (Figure S5). The absolute magnitude of  $E_{abs}$  and MAC values discussed here now will focus on the size range from 80 nm to 500 nm and 180 nm to 300 nm. The size range 80 nm to 500 nm indicates the upper limit of  $E_{abs}$  and MAC possibly over estimated due to the missing part of mixing state information in the lower size ranges as discussed. The size range of 180–300 nm indicates the lower range of corresponding  $E_{abs}$  and MAC values.



During the polluted conditions during the initial phase of the campaign,  $E_{abs}$  ranges is ~1.1 - 1.4 (Figure 9a) influenced predominantly by continental or anthropogenically processed air masses. The corresponding estimated 570 MAC range from 6.6 - 8  $m^2 g^{-1}$  (Figure 9b). Interestingly, the light absorption enhancement of rBC and MAC remained low during warm-air-mass intrusions with predominant influence of biomass burning/gas flare emissions during WA1 ( $E_{abs}$  ~1 - 1.2, MAC ~ 6.5 - 8) than under pristine background conditions ( $E_{abs}$  ~1.1 - 1.6, MAC ~ 6.5- 8.7), underscoring a strong dependence of rBC radiative effects in the central Arctic on source regions and aging/processing during long-range transport. The estimated  $E_{abs}$  during WA2 with significantly processed 575 aged rBCs are higher than those during WA1 (~1.1 - 1.5). This suggests that the rBC particles during WA2 were likely more photochemically aged, acquiring thicker coatings through prolonged exposure to condensable vapors as they traveled across pristine Arctic regions. Such aging processes promote the formation of secondary aerosols and internal mixing, ultimately enhancing light absorption even in relatively clean air masses. The observed tendencies emphasize the importance of CT as a proxy for particle aging and internal mixing, both of which 580 directly influence absorption enhancement via the lensing effect. These observations indicate that, even with limited aging and reduced condensation of secondary species during transport through relatively clean environments, warm air mass intrusions carrying biomass-burning plumes can enhance light absorption in the Arctic marine boundary layer. However, between the two warm air mass intrusion cases, WA2 showed an even 585 higher  $E_{abs}$  than WA1, due to the more aged aerosol conditions. The size resolved coating information on rBC particles is therefore essential for interpreting the degree of rBC aging across different air mass regimes.

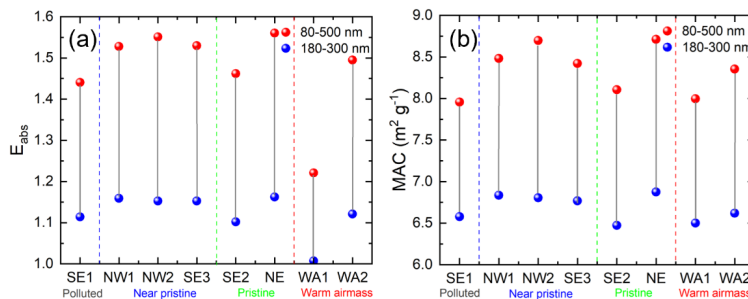


**Figure 9:** Estimated absorption enhancement ( $E_{abs}$ ) and mass absorption cross section of refractory black carbon particles for each regime for the rBC core size ranges (a) 80-500 nm and, (b) 180-300 nm.

The size resolved variation in  $E_{abs}$ , MAC, and coating thickness across different air masses has critical implications 590 for understanding the radiative impacts of BC in the Arctic. Highly coated BC particles can significantly increase shortwave radiation absorption, contributing to local atmospheric warming and potential feedbacks through snow and sea-ice albedo reduction. The pronounced absorption enhancement observed during WA1 suggests that continental or anthropogenically influenced air masses, though less frequent can be major contributors to BC radiative forcing in the Arctic MBL. Nonetheless, several limitations should be acknowledged. Mie theory, used 595 for estimating  $E_{abs}$  assumes spherical core-shell morphology, which may not accurately capture the irregular or fractal shapes of ambient BC aggregates, particularly in fresh emissions. Moreover, the composition of the coatings, especially the presence of light-absorbing organics such as brown carbon, is not explicitly resolved in MAC calculations, though it can substantially influence absorption. Overall, the observed heterogeneity in rBC optical properties across air-mass regimes underscores the need for dynamic, region-specific parameterizations in 600



600 climate models. Relying on constant enhancement factors or bulk MAC values across different transport conditions risks oversimplifying the real variability. It could lead to significant uncertainties in estimates of BC direct radiative forcing. The strong link between coating thickness and radiative properties further underscores the importance of accurately capturing aerosol aging processes when modeling BC's role in the Arctic climate. These findings provide essential observational constraints for climate models and underscore the need to 605 incorporate rBC mixing state and size-resolved properties into Arctic radiative effect assessments.

#### 4. Conclusion

610 To understand the microphysical properties and mixing state of atmospheric refractory black carbon aerosols in the central Arctic marine boundary layer, we conducted measurements on board the RV *Polarstern* during the ATWAICE campaign in summer 2022. This study provides new insights into the spatial and temporal variability of microphysical properties, mixing state, and radiative behavior of rBC aerosols in the central Arctic marine boundary layer during the summer melt season. We examined the characteristics of rBC particles across a range of synoptic regimes defined by air mass source regions, surface types, and transport histories. Our results reveal that air mass origin and atmospheric processing strongly govern rBC abundance, size, and coating characteristics.

615 rBC mass concentrations, size distributions, and coatings varied distinctly across synoptic regimes, from continental and biomass-burning influenced air masses with higher concentrations and larger cores to pristine marine regimes with extremely low rBC loadings and moderately coated particles. Despite long-range transport, coatings on rBC particles remained unexpectedly lower, likely due to limited condensable material, weak secondary aerosol formation, and efficient wet scavenging in the humid Arctic boundary layer. The limited availability of condensable material, reduced secondary aerosol formation, and the frequent occurrence of 620 persistent fog and low-level clouds likely contribute to the observed thinner coatings. Furthermore, efficient in-cloud and below-cloud scavenging of heavily coated, hydrophilic particles may further reduce the coating thickness within the observed rBC population. The observed contrasts between continental, marine, and biomass-burning influenced warm air masses emphasize that rBC aging and internal mixing are highly nonuniform under Arctic summer conditions.

625 Regions influenced by south-easterly air mass advection, characterized by stronger continental influence, exhibited relatively higher coating thicknesses for smaller rBC cores. In contrast, northerly advections associated with pristine marine environments were dominated by larger rBC particles, which also showed comparatively higher coating thicknesses. Air masses affected by continental outflows and biomass burning (particularly during warm airmass intrusion, WA1) carried elevated rBC concentrations and displayed larger mass median diameters 630 (MMDs, ~264 nm). In comparison, air masses that primarily traversed the central Arctic Ocean and consolidated sea-ice regions (NE) reflected near-pristine conditions, with minimal rBC concentrations ( $<0.6 \text{ ng m}^{-3}$ ) and only moderately coated particles. The open-oceanic regimes (SE2, SE3) exhibited intermediate characteristics, indicating rBC populations that were relatively aged and moderately coated, likely shaped by extended atmospheric residence times and interactions within the marine boundary layer. The clear contrast between 635 biomass burning/gas flaring influenced air masses (e.g., WA1) and pristine marine regimes (e.g., NE) highlights that even aged rBC particles can remain only partially internally mixed under Arctic summer conditions.



The size-resolved analysis of light absorption properties of individual rBC particles revealed substantial variability in both the absorption enhancement factor ( $E_{abs}$ ) and the mass absorption cross-section (MAC), parameters that are highly sensitive to the degree of internal mixing and coating thickness. The near pristine and pristine regimes, 640 exhibited elevated  $E_{abs}$  and MAC, indicative of more internally mixed or aged particles. In contrast, the biomass-burning-influenced regime WA1, associated with warm air mass intrusions, showed comparatively lower  $E_{abs}$ , suggesting the presence of less-aged particles or limited secondary processing during transport. Interestingly, the WA2 regime, though not directly influenced by biomass burning, showed higher  $E_{abs}$  than WA1, suggesting that the nature of the airmass transport pathway, particularly its passage over marine or relatively clean environments, 645 can facilitate prolonged aging and coating development even in the absence of strong primary sources.

These findings highlight the complex behavior of rBC in the summer Arctic, modulated by the interplay of atmospheric transport and source characteristics. The results emphasize that fixed, generalized MAC or  $E_{abs}$  values are inadequate for Arctic conditions. Instead, regime-specific, size-resolved, and mixing-state-dependent representations are essential for improving model accuracy. Given the Arctic's high sensitivity to radiative forcing 650 from absorbing aerosols, accurate characterization of rBC microphysical properties is vital for reducing uncertainties in climate projections.

#### Acknowledgement

We gratefully acknowledge the funding by the German Research Foundation, DFG grants WE 2757/6-1 and HE 5214/10-1. We gratefully acknowledge the funding by the Deutsche Forschungsgemeinschaft (DFG, German 655 Research Foundation) through the Transregional Collaborative Research Centre TRR-172 'ArctiC Amplification: Climate Relevant Atmospheric and SurfaCe Processes, and Feedback Mechanisms (AC)3' (grant 268020496). We thank Dr. Heike Wex and Dr. Holger Siebert (Leibniz Institute for Tropospheric Research, Germany) for the helpful suggestions and comments on improving this paper. We also thank Dr. Bruna A. Holanda (Hessian Agency for Nature Conservation, Environment and Geology, Germany) for her support during this study. We thank 660 everyone involved in the expedition of the research vessel *Polarstern* during ATWAICE in 2022 (Grant No. AWI\_PS131\_11 (Alfred-Wegener-Institut Helmholtz-Zentrum für Polar- und Meeresforschung, 2017). We thank the Institute of Environmental Physics, University of Bremen, for the provision of the merged MODIS-AMSR2 sea-ice concentration data at [https://data.seaice.uni-bremen.de/modis\\_amsr2](https://data.seaice.uni-bremen.de/modis_amsr2) (last access 15.10.2023). We acknowledge the use of Grammarly during the preparation of this paper.

#### 665 Data availability

Data are available upon request from the corresponding author (arun.babu@tropos.de).

#### Competing Interests

At least one of the (co-) authors is a member of the editorial board of Atmospheric Chemistry and Physics.

#### Author contributions

670 BSA, TM, MLP, BW conceptualized the study. BSA, SL, PO conducted onboard measurements. BSA, TM, MvP performed data processing. AW, JR provided the radiometer datasets. BSA prepared the original draft of the paper. All authors contributed to reviewing and editing the manuscript.



## References

675 Arctic Monitoring and Assessment Programme (AMAP) AMAP Assessment 2015: Black carbon and ozone as Arctic climate forcers.

Asmi, E., Backman, J., Servomaa, H., Virkkula, A., Gini, M. I., Eleftheriadis, K., Müller, T., Ohata, S., Kondo, Y., and Hyvärinen, A.: Absorption instruments inter-comparison campaign at the Arctic Pallas station, *Atmos Meas Tech*, 14, 5397-5413, <https://doi.org/10.5194/amt-14-5397-2021>, 2021.

680 Asmi, E., Sipkens, T. A., Saturno, J., Backman, J., Vasilatou, K., Weingartner, E., Keller, A., Ciupek, K., Müller, T., Babu Suja, A., Močnik, G., Drinovec, L., Eleftheriadis, K., Gini, M. I., Nowak, A., and Corbin, J. C.: Mass absorption cross-section of ambient black carbon aerosols - a review, *NPJ Clim Atmos Sci*, <https://doi.org/10.1038/s41612-025-01288-2>, 2025.

685 Backman, J., Schmeisser, L., Virkkula, A., Ogren, J. A., Asmi, E., Starkweather, S., Sharma, S., Eleftheriadis, K., Uttal, T., Jefferson, A., Bergin, M., Makshtas, A., Tunved, P., and Fiebig, M.: On Aethalometer measurement uncertainties and an instrument correction factor for the Arctic, *Atmos Meas Tech*, 10, 5039-5062, <https://doi.org/10.5194/amt-10-5039-2017>, 2017.

690 Baumgardner, D., Popovicheva, O., Allan, J., Bernardoni, V., Cao, J., Cavalli, F., Cozie, J., Diapouli, E., Eleftheriadis, K., Genberg, P. J., Gonzalez, C., Gysel, M., John, A., Kirchstetter, T. W., Kuhlbusch, T. A. J., Laborde, M., Lack, D., Müller, T., Niessner, R., Petzold, A., Piazzalunga, A., Putaud, J. P., Schwarz, J., Sheridan, P., Subramanian, R., Swietlicki, E., Valli, G., Vecchi, R., and Viana, M.: Soot reference materials for instrument calibration and intercomparisons: A workshop summary with recommendations, *Atmos Meas Tech*, 5, 1869-1887, <https://doi.org/10.5194/amt-5-1869-2012>, 2012.

Beer, E., Eisenman, I., and Wagner, T. J. W.: Polar Amplification Due to Enhanced Heat Flux Across the Halocline, *Geophys Res Lett*, 47, <https://doi.org/10.1029/2019GL086706>, 2020.

695 Birch, M. E. and Cary, R. A.: Elemental Carbon-Based Method for Monitoring Occupational Exposures to Particulate Diesel Exhaust, *Aerosol Science and Technology*, 25, 221-241, <https://doi.org/10.1080/02786829608965393>, 1996.

Bohren, C. F. and Huffman, D. R.: *Frontmatter*, in: *Absorption and Scattering of Light by Small Particles*, Wiley, <https://doi.org/10.1002/9783527618156.fmatter>, 1998.

700 Bond, T. C., Doherty, S. J., Fahey, D. W., Forster, P. M., Berntsen, T., Deangelo, B. J., Flanner, M. G., Ghan, S., Kärcher, B., Koch, D., Kinne, S., Kondo, Y., Quinn, P. K., Sarofim, M. C., Schultz, M. G., Schulz, M., Venkataraman, C., Zhang, H., Zhang, S., Bellouin, N., Guttikunda, S. K., Hopke, P. K., Jacobson, M. Z., Kaiser, J. W., Klimont, Z., Lohmann, U., Schwarz, J. P., Shindell, D., Storelvmo, T., Warren, S. G., and Zender, C. S.: Bounding the role of black carbon in the climate system: A scientific assessment, *Journal of Geophysical Research Atmospheres*, 118, 5380-5552, <https://doi.org/10.1002/jgrd.50171>, 2013.

Bozem, H., Hoor, P., Kunkel, D., Köllner, F., Schneider, J., Herber, A., Schulz, H., Richard Leaitch, W., Aliabadi, A. A., Willis, M. D., Burkart, J., and Abbatt, J. P. D.: Characterization of transport regimes and the polar dome during Arctic spring and summer using in situ aircraft measurements, *Atmos Chem Phys*, 19, 15049-15071, <https://doi.org/10.5194/acp-19-15049-2019>, 2019.

710 Ching, J., Riemer, N., and West, M.: Black carbon mixing state impacts on cloud microphysical properties: Effects of aerosol plume and environmental conditions, *J Geophys Res*, 121, 5990-6013, <https://doi.org/10.1002/2016JD024851>, 2016.

Ching, J., West, M., and Riemer, N.: Quantifying impacts of aerosol mixing state on nucleation-scavenging of black carbon aerosol particles, *Atmosphere (Basel)*, 9, <https://doi.org/10.3390/atmos910017>, 2018.

715 Croft, B., Martin, R. V., Richard Leaitch, W., Tunved, P., Breider, T. J., D'Andrea, S. D., and Pierce, J. R.: Processes controlling the annual cycle of Arctic aerosol number and size distributions, *Atmos Chem Phys*, 16, 3665-3682, <https://doi.org/10.5194/acp-16-3665-2016>, 2016.

Dada, L., Angot, H., Beck, I., Baccarini, A., Quéléver, L. L. J., Boyer, M., Laurila, T., Brasseur, Z., Jozef, G., de Boer, G., Shupe, M. D., Henning, S., Bucci, S., Dütsch, M., Stohl, A., Petäjä, T., Daellenbach, K. R., Jokinen, T.,



720 and Schmale, J.: A central arctic extreme aerosol event triggered by a warm air-mass intrusion, *Nat Commun*, 13, <https://doi.org/10.1038/s41467-022-32872-2>, 2022.

Dekoutsidis, G., Wirth, M., and Groß, S.: The effects of warm-air intrusions in the high Arctic on cirrus clouds, *Atmos Chem Phys*, 24, 5971–5987, <https://doi.org/10.5194/acp-24-5971-2024>, 2024.

725 Eleftheriadis, K., Vratolis, S., and Nyeki, S.: Aerosol black carbon in the European Arctic: Measurements at Zeppelin station, Ny-Ålesund, Svalbard from 1998-2007, *Geophys Res Lett*, 36, <https://doi.org/10.1029/2008GL035741>, 2009.

Engvall, A.-C., Krejci, R., Ström, J., Treffeisen, R., Scheele, R., Hermansen, O., and Paatero, J.: Changes in aerosol properties during spring-summer period in the Arctic troposphere, *Atmos. Chem. Phys*, 445–462 pp., 2008.

730 Fierce, L., Riemer, N., and Bond, T. C.: Explaining variance in black carbon's aging timescale, *Atmos Chem Phys*, 15, 3173–3191, <https://doi.org/10.5194/acp-15-3173-2015>, 2015.

Fierce, L., Bond, T. C., Bauer, S. E., Mena, F., and Riemer, N.: Black carbon absorption at the global scale is affected by particle-scale diversity in composition, *Nat Commun*, 7, <https://doi.org/10.1038/ncomms12361>, 2016.

735 Fierce, L., Onasch, T. B., Cappa, C. D., Mazzoleni, C., China, S., Bhandari, J., Davidovits, P., Al Fischer, D., Helgestad, T., Lambe, A. T., Sedlacek, A. J., Smith, G. D., and Wolff, L.: Radiative absorption enhancements by black carbon controlled by particle-to-particle heterogeneity in composition, *Proc Natl Acad Sci U S A*, 117, 5196–5203, <https://doi.org/10.1073/pnas.1919723117>, 2020.

Flanner, M. G.: Arctic climate sensitivity to local black carbon, *Journal of Geophysical Research Atmospheres*, 118, 1840–1851, <https://doi.org/10.1002/jgrd.50176>, 2013.

740 Gao, R. S., Schwarz, J. P., Kelly, K. K., Fahey, D. W., Watts, L. A., Thompson, T. L., Spackman, J. R., Slowik, J. G., Cross, E. S., Han, J. H., Davidovits, P., Onasch, T. B., and Worsnop, D. R.: A novel method for estimating light-scattering properties of soot aerosols using a modified single-particle soot photometer, *Aerosol Science and Technology*, 41, 125–135, <https://doi.org/10.1080/02786820601118398>, 2007.

745 Garrett, T. J., Brattström, S., Sharma, S., Worthy, D. E. J., and Novelli, P.: The role of scavenging in the seasonal transport of black carbon and sulfate to the Arctic, *Geophys Res Lett*, 38, <https://doi.org/10.1029/2011GL048221>, 2011.

Gogoi, M. M., Pandey, S. K., Arun, B. S., Nair, V. S., Thakur, R. C., Chaubey, J. P., Tiwari, A., Manoj, M. R., Kompalli, S. K., Vaishya, A., Prijith, S. S., Hegde, P., and Babu, S. S.: Long-term changes in aerosol radiative properties over Ny-Ålesund: Results from Indian scientific expeditions to the Arctic, *Polar Sci*, 30, <https://doi.org/10.1016/j.polar.2021.100700>, 2021.

750 Graham, R. M., Cohen, L., Petty, A. A., Boisvert, L. N., Rinke, A., Hudson, S. R., Nicolaus, M., and Granskog, M. A.: Increasing frequency and duration of Arctic winter warming events, *Geophys Res Lett*, 44, 6974–6983, <https://doi.org/10.1002/2017GL073395>, 2017.

Haywood, J. and Boucher, O.: Estimates of the direct and indirect radiative forcing due to tropospheric aerosols, a review, 2000.

755 Henderson, G. R., Barrett, B. S., Wachowicz, L. J., Mattingly, K. S., Preece, J. R., and Mote, T. L.: Local and Remote Atmospheric Circulation Drivers of Arctic Change: A Review, <https://doi.org/10.3389/feart.2021.709896>, 1 July 2021.

Heutte, B., Bergner, N., Beck, I., Angot, H., Dada, L., Quéléver, L. L. J., Laurila, T., Boyer, M., Brasseur, Z., Daellenbach, K. R., Henning, S., Kuang, C., Kulmala, M., Lampilahti, J., Lampimäki, M., Petäjä, T., Shupe, M. D., Sipilä, M., Uin, J., Jokinen, T., and Schmale, J.: Measurements of aerosol microphysical and chemical properties in the central Arctic atmosphere during MOSAiC, *Sci Data*, 10, <https://doi.org/10.1038/s41597-023-02586-1>, 2023.



765 Jurányi, Z., Zanatta, M., Lund, M., Samset, B., Skeie, R., Sharma, S., and Herber, A.: A climatology of Black Carbon properties in the Arctic, from a decade of spring and summertime aircraft measurements, <https://doi.org/10.21203/rs.3.rs-1938170/v1>, 11 August 2022.

Jurányi, Z., Zanatta, M., Lund, M. T., Samset, B. H., Skeie, R. B., Sharma, S., Wendisch, M., and Herber, A.: Atmospheric concentrations of black carbon are substantially higher in spring than summer in the Arctic, *Commun Earth Environ*, 4, <https://doi.org/10.1038/s43247-023-00749-x>, 2023.

770 Kanzow, T.: Berichte zur Polar- und Meeresforschung, Bericht Nr. 770/2023, [https://doi.org/10.57738/BzPM\\_0770\\_2023](https://doi.org/10.57738/BzPM_0770_2023), 2023.

Ko, J., Krasowsky, T., and Ban-Weiss, G.: Measurements to determine the mixing state of black carbon emitted from the 2017-2018 California wildfires and urban Los Angeles, *Atmos Chem Phys*, 20, 15635–15664, <https://doi.org/10.5194/acp-20-15635-2020>, 2020.

775 Kompalli, S. K., Babu, S. N. S., Krishnakumari Satheesh, S., Moorthy, K. K., Das, T., Boopathy, R., Liu, D., Darbyshire, E., Allan, J. D., Brooks, J., Flynn, M. J., and Coe, H.: Seasonal contrast in size distributions and mixing state of black carbon and its association with PM1.0 chemical composition from the eastern coast of India, *Atmos Chem Phys*, 20, 3965–3985, <https://doi.org/10.5194/acp-20-3965-2020>, 2020.

780 Kompalli, S. K., Babu, S. N. S., Moorthy, K. K., Satheesh, S. K., Gogoi, M. M., Nair, V. S., Jayachandran, V. N., Liu, D., Flynn, M. J., and Coe, H.: Mixing state of refractory black carbon aerosol in the South Asian outflow over the northern Indian Ocean during winter, *Atmos Chem Phys*, 21, 9173–9199, <https://doi.org/10.5194/acp-21-9173-2021>, 2021.

785 Laborde, M., Schnaiter, M., Linke, C., Saathoff, H., Naumann, K.-H., Möhler, O., Berlenz, S., Wagner, U., Taylor, J. W., Liu, D., Flynn, M., Allan, J. D., Coe, H., Heimerl, K., Dahlkötter, F., Weinzierl, B., Wollny, A. G., Zanatta, M., Cozic, J., Laj, P., Hitzenberger, R., Schwarz, J. P., and Gysel, M.: Single Particle Soot Photometer intercomparison at the AIDA chamber, *Atmos Meas Tech*, 5, 3077–3097, <https://doi.org/10.5194/amt-5-3077-2012>, 2012.

Laborde, M., Crippa, M., Tritscher, T., Jurányi, Z., Decarlo, P. F., Temime-Roussel, B., Marchand, N., Eckhardt, S., Stohl, A., Baltensperger, U., Prévôt, A. S. H., Weingartner, E., and Gysel, M.: Black carbon physical properties and mixing state in the European megacity Paris, *Atmos Chem Phys*, 13, 5831–5856, <https://doi.org/10.5194/acp-13-5831-2013>, 2013.

790 Lim, S., Lee, M., and Yoo, H. J.: Size distributions, mixing state, and morphology of refractory black carbon in an urban atmosphere of northeast Asia during summer, *Science of the Total Environment*, 856, <https://doi.org/10.1016/j.scitotenv.2022.158436>, 2023.

795 Liu, D., Allan, J. D., Young, D. E., Coe, H., Beddows, D., Fleming, Z. L., Flynn, M. J., Gallagher, M. W., Harrison, R. M., Lee, J., Prevot, A. S. H., Taylor, J. W., Yin, J., Williams, P. I., and Zotter, P.: Size distribution, mixing state and source apportionment of black carbon aerosol in London during winter time, *Atmos Chem Phys*, 14, 10061–10084, <https://doi.org/10.5194/acp-14-10061-2014>, 2014.

800 Liu, D., Quennehen, B., Darbyshire, E., Allan, J. D., Williams, P. I., Taylor, J. W., J.-B. Bauguitte, S., Flynn, M. J., Lowe, D., Gallagher, M. W., Bower, K. N., Choularton, T. W., and Coe, H.: The importance of Asia as a source of black carbon to the European Arctic during springtime 2013, *Atmos Chem Phys*, 15, 11537–11555, <https://doi.org/10.5194/acp-15-11537-2015>, 2015.

805 Liu, D., Joshi, R., Wang, J., Yu, C., Allan, J. D., Coe, H., Flynn, M. J., Xie, C., Lee, J., Squires, F., Kotthaus, S., Grimmond, S., Ge, X., Sun, Y., and Fu, P.: Contrasting physical properties of black carbon in urban Beijing between winter and summer, *Atmos Chem Phys*, 19, 6749–6769, <https://doi.org/10.5194/acp-19-6749-2019>, 2019.

Liu, J., Fan, S., Horowitz, L. W., and Levy, H.: Evaluation of factors controlling long-range transport of black carbon to the Arctic, *Journal of Geophysical Research Atmospheres*, 116, <https://doi.org/10.1029/2010JD015145>, 2011.



810 Ludwig, V., Spreen, G., and Pedersen, L. T.: Evaluation of a new merged sea-ice concentration dataset at 1 km resolution from thermal infrared and passive microwave satellite data in the arctic, *Remote Sens.*, 12, 1–28, <https://doi.org/10.3390/rs12193183>, 2020.

815 Matsui, H.: Black carbon simulations using a size- and mixing-state-resolved three-dimensional model: 1. Radiative effects and their uncertainties, *J Geophys Res.*, 121, 1793–1807, <https://doi.org/10.1002/2015JD023998>, 2016.

McMeeking, G. R., Hamburger, T., Liu, D., Flynn, M., Morgan, W. T., Northway, M., Highwood, E. J., Krejci, R., Allan, J. D., Minikin, A., and Coe, H.: Black carbon measurements in the boundary layer over western and northern Europe, *Atmos Chem Phys.*, 10, 9393–9414, <https://doi.org/10.5194/acp-10-9393-2010>, 2010.

820 Mortin, J., Svensson, G., Graversen, R. G., Kapsch, M. L., Stroeve, J. C., and Boisvert, L. N.: Melt onset over Arctic sea ice controlled by atmospheric moisture transport, *Geophys Res Lett.*, 43, 6636–6642, <https://doi.org/10.1002/2016GL069330>, 2016.

Moteki, N., Kondo, Y., and Nakamura, S. ichi: Method to measure refractive indices of small nonspherical particles: Application to black carbon particles, *J Aerosol Sci.*, 41, 513–521, <https://doi.org/10.1016/j.jaerosci.2010.02.013>, 2010.

825 Moteki, N. and Kondo, Y.: Dependence of laser-induced incandescence on physical properties of black carbon aerosols: Measurements and theoretical interpretation, *Aerosol Science and Technology*, 44, 663–675, <https://doi.org/10.1080/02786826.2010.484450>, 2010.

830 Moteki, N., Kondo, Y., Oshima, N., Takegawa, N., Koike, M., Kita, K., Matsui, H., and Kajino, M.: Size dependence of wet removal of black carbon aerosols during transport from the boundary layer to the free troposphere, *Geophys Res Lett.*, 39, <https://doi.org/10.1029/2012GL052034>, 2012.

Moteki, N., Ohata, S., Yoshida, A., and Adachi, K.: Constraining the complex refractive index of black carbon particles using the complex forward-scattering amplitude, *Aerosol Science and Technology*, 57, 678–699, <https://doi.org/10.1080/02786826.2023.2202243>, 2023.

835 Motos, G., Schmale, J., Corbin, J. C., Zanatta, M., Baltensperger, U., and Gysel-Beer, M.: Droplet activation behaviour of atmospheric black carbon particles in fog as a function of their size and mixing state, *Atmos Chem Phys.*, 19, 2183–2207, <https://doi.org/10.5194/acp-19-2183-2019>, 2019a.

840 Motos, G., Schmale, J., Corbin, J. C., Modini, R. L., Karlen, N., Bertò, M., Baltensperger, U., and Gysel-Beer, M.: Cloud droplet activation properties and scavenged fraction of black carbon in liquid-phase clouds at the high-alpine research station Jungfraujoch (3580 m.a.s.l.), *Atmos Chem Phys.*, 19, 3833–3855, <https://doi.org/10.5194/acp-19-3833-2019>, 2019b.

Motos, G., Corbin, J. C., Schmale, J., Modini, R. L., Bertò, M., Kupiszewski, P., Baltensperger, U., and Gysel-Beer, M.: Black Carbon Aerosols in the Lower Free Troposphere are Heavily Coated in Summer but Largely Uncoated in Winter at Jungfraujoch in the Swiss Alps, *Geophys Res Lett.*, 47, <https://doi.org/10.1029/2020GL088011>, 2020.

845 Müller, K., Lehmann, S., Van Pinxteren, D., Gnauk, T., Niedermeier, N., Wiedensohler, A., and Herrmann, H.: Atmospheric Chemistry and Physics Particle characterization at the Cape Verde atmospheric observatory during the 2007 RHaMBLe intensive, *Atmos. Chem. Phys.*, 2709–2721 pp., 2010.

Müller, T., Laborde, M., Kassell, G., and Wiedensohler, A.: Design and performance of a three-wavelength LED-based total scatter and backscatter integrating nephelometer, *Atmos Meas Tech.*, 4, 1291–1303, <https://doi.org/10.5194/amt-4-1291-2011>, 2011.

Nenes, A., Conant, W. C., and Seinfeld, J. H.: Black carbon radiative heating effects on cloud microphysics and implications for the aerosol indirect effect 2. Cloud microphysics, *Journal of Geophysical Research: Atmospheres*, 107, <https://doi.org/10.1029/2002jd002101>, 2002.

855 Pandolfi, M., Alados-Arboledas, L., Alastuey, A., Andrade, M., Angelov, C., Artiñano, B., Backman, J., Baltensperger, U., Bonasoni, P., Bukowiecki, N., Collaud Coen, M., Conil, S., Coz, E., Crenn, V., Dudoitidis, V., Ealo, M., Eleftheriadis, K., Favez, O., Fefatidis, P., Fiebig, M., Flentje, H., Ginot, P., Gysel, M., Henzing, B.,



860 Hoffer, A., Holubova Smejkalova, A., Kalapov, I., Kalivitis, N., Kouvarakis, G., Kristensson, A., Kulmala, M., Lihavainen, H., Lunder, C., Luoma, K., Lyamani, H., Marinoni, A., Mihalopoulos, N., Moerman, M., Nicolas, J., O'Dowd, C., Petäjä, T., Petit, J. E., Marc Pichon, J., Prokopiuk, N., Putaud, J. P., Rodríguez, S., Sciare, J., Sellegrí, K., Swietlicki, E., Titos, G., Tuch, T., Tunved, P., Ulevicius, V., Vaishya, A., Vana, M., Virkkula, A., Vratolis, S., Weingartner, E., Wiedensohler, A., and Laj, P.: A European aerosol phenomenology - 6: Scattering properties of atmospheric aerosol particles from 28 ACTRIS sites, *Atmos Chem Phys*, 18, 7877–7911, <https://doi.org/10.5194/acp-18-7877-2018>, 2018.

865 Park, J., Dall'osto, M., Park, K., Gim, Y., Jin Kang, H., Jang, E., Park, K. T., Park, M., Soo Yum, S., Jung, J., Yong Lee, B., and Jun Yoon, Y.: Shipborne observations reveal contrasting Arctic marine, Arctic terrestrial and Pacific marine aerosol properties, *Atmos Chem Phys*, 20, 5573–5590, <https://doi.org/10.5194/acp-20-5573-2020>, 2020.

870 Pernov, J. B., Beddows, D., Thomas, D. C., Dall'osto, M., Harrison, R. M., Schmale, J., Skov, H., and Massling, A.: Increased aerosol concentrations in the High Arctic attributable to changing atmospheric transport patterns, *NPJ Clim Atmos Sci*, 5, <https://doi.org/10.1038/s41612-022-00286-y>, 2022.

875 Petzold, A. and Schönlinner, M.: Multi-angle absorption photometry - A new method for the measurement of aerosol light absorption and atmospheric black carbon, *J Aerosol Sci*, 35, 421–441, <https://doi.org/10.1016/j.jaerosci.2003.09.005>, 2004.

880 Popovicheva, O. B., Evangelou, N., Eleftheriadis, K., Kalogridis, A. C., Sitnikov, N., Eckhardt, S., and Stohl, A.: Black Carbon Sources Constrained by Observations in the Russian High Arctic, *Environ Sci Technol*, 51, 3871–3879, <https://doi.org/10.1021/acs.est.6b05832>, 2017.

885 Quinn, P. K., Miller, T. L., Bates, T. S., Ogren, J. A., Andrews, E., and Shaw, G. E.: A 3-year record of simultaneously measured aerosol chemical and optical properties at Barrow, Alaska, *Journal of Geophysical Research: Atmospheres*, 107, <https://doi.org/10.1029/2001jd001248>, 2002.

890 Quinn, P. K., Bates, T. S., Baum, E., Doubleday, N., Fiore, A. M., Flanner, M., Fridlind, A., Garrett, T. J., Koch, D., Menon, S., Shindell, D., Stohl, A., and Warren, S. G.: Short-lived pollutants in the Arctic: their climate impact and possible mitigation strategies, *Atmos. Chem. Phys*, 1723–1735 pp., 2008.

895 Raatikainen, T., Brus, D., Hyvärinen, A. P., Svensson, J., Asmi, E., and Lihavainen, H.: Black carbon concentrations and mixing state in the Finnish Arctic, *Atmos Chem Phys*, 15, 10057–10070, <https://doi.org/10.5194/acp-15-10057-2015>, 2015.

Rantanen, M., Karpechko, A. Y., Lipponen, A., Nordling, K., Hyvärinen, O., Ruosteenoja, K., Vihma, T., and Laaksonen, A.: The Arctic has warmed nearly four times faster than the globe since 1979, *Commun Earth Environ*, 3, <https://doi.org/10.1038/s43247-022-00498-3>, 2022.

Rose, T., Crewell, S., Löhner, U., and Simmer, C.: A network suitable microwave radiometer for operational monitoring of the cloudy atmosphere, *Atmos Res*, 75, 183–200, <https://doi.org/10.1016/j.atmosres.2004.12.005>, 2005.

Sand, M., Berntsen, T. K., Seland, Ø., and Kristjánsson, J. E.: Arctic surface temperature change to emissions of black carbon within Arctic or midlatitudes, *Journal of Geophysical Research Atmospheres*, 118, 7788–7798, <https://doi.org/10.1002/jgrd.50613>, 2013.

895 Schmale, J., Arnold, S. R., Law, K. S., Thorp, T., Anenberg, S., Simpson, W. R., Mao, J., and Pratt, K. A.: Local Arctic Air Pollution: A Neglected but Serious Problem, *Earths Future*, 6, 1385–1412, <https://doi.org/10.1029/2018EF000952>, 2018.

Schmale, J., Zieger, P., and Ekman, A. M. L.: Aerosols in current and future Arctic climate, *Nat Clim Chang*, 11, 95–105, <https://doi.org/10.1038/s41558-020-00969-5>, 2021.

900 Schmale, J., Sharma, S., Decesari, S., Pernov, J., Massling, A., Hansson, H. C., Von Salzen, K., Skov, H., Andrews, E., Quinn, P. K., Upchurch, L. M., Eleftheriadis, K., Traversi, R., Gilardoni, S., Mazzola, M., Laing, J., and Hopke, P.: Pan-Arctic seasonal cycles and long-term trends of aerosol properties from 10 observatories, *Atmos Chem Phys*, 22, 3067–3096, <https://doi.org/10.5194/acp-22-3067-2022>, 2022.



905 Schmeisser, L., Backman, J., Ogren, J. A., Andrews, E., Asmi, E., Starkweather, S., Uttal, T., Fiebig, M., Sharma, S., Eleftheriadis, K., Vratolis, S., Bergin, M., Tunved, P., and Jefferson, A.: Seasonality of aerosol optical properties in the Arctic, *Atmos Chem Phys*, 18, 11599–11622, <https://doi.org/10.5194/acp-18-11599-2018>, 2018.

Schnaiter, M., Linke, C., Möhler, O., Naumann, K. H., Saathoff, H., Wagner, R., Schurath, U., and Wehner, B.: Absorption amplification of black carbon internally mixed with secondary organic aerosol, *Journal of Geophysical Research D: Atmospheres*, 110, 1–11, <https://doi.org/10.1029/2005JD006046>, 2005.

910 Schulz, H., Zanatta, M., Bozem, H., Richard Leaitch, W., Herber, A. B., Burkart, J., Willis, M. D., Kunkel, D., Hoor, P. M., Abbatt, J. P. D., and Gerdes, R.: High Arctic aircraft measurements characterising black carbon vertical variability in spring and summer, *Atmos Chem Phys*, 19, 2361–2384, <https://doi.org/10.5194/acp-19-2361-2019>, 2019.

Schwarz, J. P., Gao, R. S., Spackman, J. R., Watts, L. A., Thomson, D. S., Fahey, D. W., Ryerson, T. B., Peischl, J., Holloway, J. S., Trainer, M., Frost, G. J., Baynard, T., Lack, D. A., de Gouw, J. A., Warneke, C., and Del Negro, L. A.: Measurement of the mixing state, mass, and optical size of individual black carbon particles in urban and biomass burning emissions, *Geophys Res Lett*, 35, <https://doi.org/10.1029/2008GL033968>, 2008.

915 Sharma, S., Andrews, E., Barrie, L. A., Ogren, J. A., and Lavoué, D.: Variations and sources of the equivalent black carbon in the high Arctic revealed by long-term observations at Alert and Barrow: 1989–2003, *Journal of Geophysical Research Atmospheres*, 111, <https://doi.org/10.1029/2005JD006581>, 2006.

Shiraiwa, M., Kondo, Y., Moteki, N., Takegawa, N., Miyazaki, Y., and Blake, D. R.: Evolution of mixing state of black carbon in polluted air from Tokyo, *Geophys Res Lett*, 34, <https://doi.org/10.1029/2007GL029819>, 2007.

Spreen, G., Kaleschke, L., and Heygster, G.: Sea ice remote sensing using AMSR-E 89-GHz channels, *J Geophys Res Oceans*, 113, <https://doi.org/10.1029/2005JC003384>, 2008.

920 Stein, A. F., Draxler, R. R., Rolph, G. D., Stunder, B. J. B., Cohen, M. D., and Ngan, F.: Noaa's hysplit atmospheric transport and dispersion modeling system, <https://doi.org/10.1175/BAMS-D-14-00110.1>, 1 December 2015.

Stohl, A.: Characteristics of atmospheric transport into the Arctic troposphere, *Journal of Geophysical Research Atmospheres*, 111, <https://doi.org/10.1029/2005JD006888>, 2006.

925 Stohl, A., Klimont, Z., Eckhardt, S., Kupiainen, K., Shevchenko, V. P., Kopeikin, V. M., and Novigatsky, A. N.: Black carbon in the Arctic: The underestimated role of gas flaring and residential combustion emissions, *Atmos Chem Phys*, 13, 8833–8855, <https://doi.org/10.5194/acp-13-8833-2013>, 2013.

Taketani, F., Miyakawa, T., Takashima, H., Komazaki, Y., Pan, X., Kanaya, Y., and Inoue, J.: Shipborne observations of atmospheric black carbon aerosol particles over the Arctic Ocean, Bering Sea, and North Pacific Ocean during september 2014, *J Geophys Res*, 121, 1914–1921, <https://doi.org/10.1002/2015JD023648>, 2016.

930 Taylor, J. W., Allan, J. D., Allen, G., Coe, H., Williams, P. I., Flynn, M. J., Le Breton, M., Muller, J. B. A., Percival, C. J., Oram, D., Forster, G., Lee, J. D., Rickard, A. R., Parrington, M., and Palmer, P. I.: Size-dependent wet removal of black carbon in Canadian biomass burning plumes, *Atmos Chem Phys*, 14, 13755–13771, <https://doi.org/10.5194/acp-14-13755-2014>, 2014.

935 Thackeray, C. W. and Hall, A.: An emergent constraint on future Arctic sea-ice albedo feedback, *Nat Clim Change*, 9, 972–978, <https://doi.org/10.1038/s41558-019-0619-1>, 2019.

Tomasi, C., Vitale, V., Lupi, A., Di Carmine, C., Campanelli, M., Herber, A., Treffeisen, R., Stone, R. S., Andrews, E., Sharma, S., Radionov, V., von Hoyningen-Huene, W., Stebel, K., Hansen, G. H., Myhre, C. L., Wehrli, C., Aaltonen, V., Lihavainen, H., Virkkula, A., Hillamo, R., Ström, J., Toledano, C., Cachorro, V. E., Ortiz, P., de Frutos, A. M., Blindheim, S., Frioud, M., Gausa, M., Zielinski, T., Petelski, T., and Yamanouchi, T.: Aerosols in polar regions: A historical overview based on optical depth and in situ observations, <https://doi.org/10.1029/2007JD008432>, 27 August 2007.

Tunved, P., Ström, J., and Krejci, R.: Arctic aerosol life cycle: Linking aerosol size distributions observed between 2000 and 2010 with air mass transport and precipitation at Zeppelin station, Ny-Ålesund, Svalbard, *Atmos Chem Phys*, 13, 3643–3660, <https://doi.org/10.5194/acp-13-3643-2013>, 2013.

950



Walbröl, A., Crewell, S., Engelmann, R., Orlandi, E., Griesche, H., Radenz, M., Hofer, J., Althausen, D., Maturilli, M., and Ebelt, K.: Atmospheric temperature, water vapour and liquid water path from two microwave radiometers during MOSAiC, *Sci Data*, 9, <https://doi.org/10.1038/s41597-022-01504-1>, 2022.

955 Wendisch, M., Brückner, M., Crewell, S., Ehrlich, A., Notholt, J., Lüpkes, C., Macke, A., Burrows, J. P., Rinke, A., Quaas, J., Maturilli, M., Schemann, V., Shupe, M. D., Akansu, E. F., et al.: Atmospheric and Surface Processes, and Feedback Mechanisms Determining Arctic Amplification, *Bull Am Meteorol Soc*, 104, E208–E242, <https://doi.org/10.1175/BAMS-D-21-0218.1>, 2023.

960 Winiger, P., Andersson, A., Eckhardt, S., Stohl, A., Semiletov, I. P., Dudarev, O. V., Charkin, A., Shakhova, N., Klimont, Z., Heyes, C., and Gustafsson, Ö.: Siberian Arctic black carbon sources constrained by model and observation, *Proc Natl Acad Sci U S A*, 114, E1054–E1061, <https://doi.org/10.1073/pnas.1613401114>, 2017.

965 Woods, C. and Caballero, R.: The role of moist intrusions in winter arctic warming and sea ice decline, *J Clim*, 29, 4473–4485, <https://doi.org/10.1175/JCLI-D-15-0773.1>, 2016.

970 Yang, Y., Müller, T., Poulain, L., Atabakhsh, S., Holanda, B. A., Voigtlander, J., Arora, S., and Pöhlker, M. L.: Microphysical properties of refractory black carbon aerosols for different air masses at a central European background site, *Atmos Chem Phys*, 25, 8637–8655, <https://doi.org/10.5194/acp-25-8637-2025>, 2025.

975 Yang, Y. (2024). Assessing Absorption Enhancement in Black Carbon: Insights into Mixing State Heterogeneity. Zenodo. <https://doi.org/10.5281/zenodo.17312995>

980 Zanatta, M., Laj, P., Gysel, M., Baltensperger, U., Vratolis, S., Eleftheriadis, K., Kondo, Y., Dubuisson, P., Winiarek, V., Kazadzis, S., Tunved, P., and Jacobi, H. W.: Effects of mixing state on optical and radiative properties of black carbon in the European Arctic, *Atmos Chem Phys*, 18, 14037–14057, <https://doi.org/10.5194/acp-18-14037-2018>, 2018.

985 Zanatta, M., Mertes, S., Jourdan, O., Dupuy, R., Järvinen, E., Schnaiter, M., Eppers, O., Schneider, J., Jurányi, Z., and Herber, A.: Airborne investigation of black carbon interaction with low-level, persistent, mixed-phase clouds in the Arctic summer, *Atmos Chem Phys*, 23, 7955–7973, <https://doi.org/10.5194/acp-23-7955-2023>, 2023.

Zeng, L., Tan, T., Zhao, G., Du, Z., Hu, S., Shang, D., and Hu, M.: Overestimation of black carbon light absorption due to mixing state heterogeneity, *NPJ Clim Atmos Sci*, 7, <https://doi.org/10.1038/s41612-023-00535-8>, 2024.

Zhai, J., Yang, X., Li, L., Bai, B., Liu, P., Huang, Y., Fu, T. M., Zhu, L., Zeng, Z., Tao, S., Lu, X., Ye, X., Wang, X., Wang, L., and Chen, J.: Absorption Enhancement of Black Carbon Aerosols Constrained by Mixing-State Heterogeneity, *Environ Sci Technol*, 56, 1586–1593, <https://doi.org/10.1021/acs.est.1c06180>, 2022.

Zhang, Y., Cheng, X., Liu, J., and Hui, F.: The potential of sea ice leads as a predictor for summer Arctic sea ice extent, *Cryosphere*, 12, 3747–3757, <https://doi.org/10.5194/tc-12-3747-2018>, 2018.

990 Zhang, Y., Favez, O., Canonaco, F., Liu, D., Močnik, G., Amodeo, T., Sciare, J., Prévôt, A. S. H., Gros, V., and Albinet, A.: Evidence of major secondary organic aerosol contribution to lensing effect black carbon absorption enhancement, *NPJ Clim Atmos Sci*, 1, <https://doi.org/10.1038/s41612-018-0056-2>, 2018.

Zhao, C. and Garrett, T. J.: Effects of Arctic haze on surface cloud radiative forcing, *Geophys Res Lett*, 42, 557–564, <https://doi.org/10.1002/2014GL062015>, 2015.

Zieger, P., Heslin-Rees, D., Karlsson, L., Koike, M., Modini, R., and Krejci, R.: Black carbon scavenging by low-level Arctic clouds, *Nat Commun*, 14, <https://doi.org/10.1038/s41467-023-41221-w>, 2023.